

การจำลองการเกิดไฮเปอร์นิวเคลียสในการเหนี่ยวนำปฏิกิริยาไฮเปอร์รอน

นายอายุท ลิมพิรัตน์

วิทยานิพนธ์นี้เป็นส่วนหนึ่งของการศึกษาตามหลักสูตรปริญญาวิทยาศาสตรดุษฎีบัณฑิต

สาขาวิชาฟิสิกส์

มหาวิทยาลัยเทคโนโลยีสุรนารี

ปีการศึกษา 2551

**SIMULATION OF HYPERNUCLEUS
PRODUCTION IN HYPERON
INDUCED REACTIONS**

Ayut Liphirat

A Thesis Submitted in Partial Fulfillment of the Requirements for the

Degree of Doctor of Philosophy in Physics

Suranaree University of Technology

Academic Year 2008

SIMULATION OF HYPERNUCLEUS PRODUCTION IN HYPERON INDUCED REACTIONS

Suranaree University of Technology has approved this thesis submitted in partial fulfillment of the requirements for the Degree of Doctor of Philosophy.

Thesis Examining Committee

(Prof. Dr. Prasart Suebka)

Chairperson

(Asst. Prof. Dr. Chinorat Kobdaj)

Member (Thesis Advisor)

(Prof. Dr. Yupeng Yan)

Member

(Asst. Prof. Col. Dr. Worasit Uchai)

Member

(Asst. Prof. Dr. Viroj Limkaisang)

Member

(Prof. Dr. Pairote Sattayatham)

Vice Rector for Academic Affairs

(Assoc. Prof. Dr. Prapan Manyum)

Dean of Institute of Science

อายุทธ ลิมพิรัตน์ : การจำลองการเกิดไฮเปอร์นิวเคลียสในการเหนี่ยวนำปฏิกิริยา
ไฮเปอร์รอน (SIMULATION OF HYPERNUCLEUS PRODUCTION IN
HYPERON INDUCED REACTIONS) อาจารย์ที่ปรึกษา : ผู้ช่วยศาสตราจารย์ ดร.
ชิโนรัตน์ กอบเดช, 103 หน้า.

ในการศึกษานี้แบบจำลองพลศาสตร์ควอนตัมเชิงโมเลกุลเหนือสัมพัทธภาพถูกนำมาใช้เพื่อศึกษาอันตรกิริยาของแอนติโปรตอน-นิวเคลียสในการอธิบายปริมาณผลิตผลผลิต การแจกแจงโมเมนตัมตามขวาง การแจกแจงราฟิดิตี โดยมุ่งเน้นไปที่การเกิดอนุภาคชนิดสเตรนจ์ซึ่งเป็นปัจจัยสำคัญต่อการเกิดไฮเปอร์นิวเคลียส ผลการศึกษาการเกิดอนุภาคชนิดสเตรนจ์ประเภทเคออนแลมบ์ดาและแอนติแลมบ์ดาจากปฏิกิริยาระหว่างแอนติโปรตอนกับนิวเคลียสของลิเทียม คาร์บอน ซัลเฟอร์ ทองแดงและซีออน แล้วเปรียบเทียบกับผลการทดลองพบว่าแบบจำลองพลศาสตร์ควอนตัมเชิงโมเลกุลเหนือสัมพัทธภาพสามารถอธิบายการเกิดอนุภาคดังกล่าวได้สอดคล้องกับผลการทดลองเป็นอย่างดี จากนั้นได้นำแบบจำลองพลศาสตร์ควอนตัมเชิงโมเลกุลเหนือสัมพัทธภาพไปศึกษาเงื่อนไขในการเกิดไฮเปอร์นิวเคลียสจากปฏิกิริยาระหว่างแอนติโปรตอนกับนิวเคลียสของทองที่พลังงานศูนย์กลางมวล 3 ถึง 4 จิกะอิเล็กตรอนโวลต์ จากการศึกษาพบว่า ผลิตผลผลิตของคูเคออนจะสูงกว่าการเกิดอนุภาคแอนติไซซึ่งหมายถึงสามารถใช้คูเคออนสำหรับเป็นดัชนีการเกิดอนุภาคไซได้เป็นอย่างดี ทั้งนี้จะเกิดคูเคออนที่โมเมนตัม 0.3 GeV/c จำนวนมากที่สุด ซึ่งพบได้จากการพิจารณาปริมาณการแจกแจงโมเมนตัม นอกจากนี้ อนุภาคไซที่เกิดขึ้นจากปฏิกิริยาระหว่างแอนติโปรตอนกับนิวเคลียสของทองส่วนใหญ่จะมีโมเมนตัม 0.2 GeV/c ซึ่งน้อยกว่าโมเมนตัมเฉลี่ยของอนุภาคไซที่เกิดจากปฏิกิริยาระหว่างแอนติโปรตอนกับโปรตอน นั้นหมายถึงอนุภาคไซจากปฏิกิริยาระหว่างแอนติโปรตอนกับนิวเคลียสของทองจะถูกหน่วงโดยการกระเจิงเข้าไปในนิวเคลียสปฐมภูมิโดยสามารถยืนยันได้จากการศึกษาการแจกแจงการกระเจิงเข้าไปของอนุภาคไซที่ระบุการกระเจิงเข้าไปของอนุภาคไซส่วนใหญ่จำนวน 3 ครั้งในนิวเคลียสปฐมภูมิ หลังจากนั้นอนุภาคไซจะถูกดูดกลืนหรือถูกหน่วงในนิวเคลียสทุติยภูมิต่อไป เงื่อนไขปฏิกิริยาดังกล่าวจะถูกทดสอบต่อไปในการทดลอง PANDA ที่ FAIR ในอนาคต

สาขาวิชาฟิสิกส์
ปีการศึกษา 2551

ลายมือชื่อนักศึกษา _____
ลายมือชื่ออาจารย์ที่ปรึกษา _____
ลายมือชื่ออาจารย์ที่ปรึกษาร่วม _____

AYUT LIMPHIRAT : SIMULATION OF HYPERNUCLEUS
PRODUCTION IN HYPERON INDUCED REACTIONS. THESIS
ADVISOR : ASST. PROF. CHINORAT KOBDAJ, Ph.D. 103 PP.

HYPERNUCLEUS/UrQMD/HYPERON/MULTIPLICITY/MOMENTUM
DISTRIBUTION

The capabilities of the Ultra-relativistic Quantum Molecular Dynamics (UrQMD) model in describing antiproton-nucleus collisions are presented. The model provides a good description of the experimental data on multiplicities, transverse momentum distributions and rapidity distributions in antiproton-nucleus collisions. Special emphasize is put on the comparison of strange particle in reactions with nuclear targets ranging from ${}^7\text{Li}$, ${}^{12}\text{C}$, ${}^{32}\text{S}$, ${}^{64}\text{Cu}$ to ${}^{131}\text{Xe}$ because important role of strangeness for the exploration of hypernuclei at PANDA-FAIR. The productions of the double strange baryons Ξ^- and Ξ^+ , which may be used to produce double Λ hypernuclei, are predicted in this work for the reactions $\bar{p} + {}^{24}\text{Mg}$, $\bar{p} + {}^{64}\text{Cu}$ and $\bar{p} + {}^{197}\text{Au}$.

We apply the UrQMD model to explore the possibilities to produce $\Lambda\Lambda$ hypernucleus in $\bar{p} + \text{nucleus}$ reactions at center-of-mass energies of 3 - 4 GeV. It is found that the multiplicities of K^+K^+ pairs are much higher than the ones of Ξ^- and are comparable to the multiplicities of Ξ^+ , and K^+K^+ pairs can be used as experimental trigger of Ξ^- productions. The K^+K^+ trigger can be easily detected at momenta around 0.3 GeV/c. The momenta of Ξ^- from the $\bar{p} + \text{Au}$ reactions are around 0.2 GeV/c, much lower than the momenta of Ξ^- from the $\bar{p} + p$ reactions. This implies that the Ξ^- s are decelerated by re-scattering inside the primary nucleus. The distribution of re-scattering numbers of Ξ^- reveals that the average number of

re-scatterings of Ξ inside the primary nucleus is three. The decelerated Ξ in the first target may be absorbed or further decelerated inside the secondary nucleus, depending on the momentum. The predictions can be tested with the planned PANDA experiment at the future FAIR facility.

School of Physics

Academic Year 2008

Student's Signature _____

Advisor's Signature _____

Co-Advisor's Signature _____

ACKNOWLEDGEMENTS

I am grateful to my thesis supervisor, Asst. Prof. Dr. Chinorat Kobdaj, and co-supervisor, Prof. Dr. Yupeng Yan, for their guidance throughout this work. They gave me a very good research experience. I have learnt not only the relevant physics but also the spiritual attitude.

I would like to thank Prof. Dr. Dr. h.c. Horst Stöcker, Prof. Dr. Marcus Bleicher and Dr. Gerhard Baur for their guidance during my research at the Institute for Theoretical Physics, Frankfurt University, Germany.

I would like to thank Prof. Dr. Prasart Suebka, Asst. Prof. Col. Dr. Worasit Uchai and Asst. Prof. Dr. Viroj Limkaisang for their kindness and being Thesis Examining Committee.

I acknowledge the financial support by Suranaree University of Technology (SUT outstanding academic performance scholarship) and the National Research Council of Thailand (NRCT) under Grant No. 1.CH5/2549.

I wish to thank Asst. Prof. Dr. Jessada Tanthanuch, Dr. Suppiya Siranan, Dr. Pornrad Srisawad, Dr. Sampart Cheedket, Dr. Khanchai Khosonthongkee, Dr. Chalump Oonariya, Dr. Chakrit Nualchimlee, Mrs. Phengkhae Phetmai and my friends for their consistent help and for all good things they gave to me.

I would like to thank my grandparents, my parents, my relative, Götting-Riesse families and Wanwisa Pattanasiriwisawa for their understanding, support and encouragement over the years of my study.

Finally, It is a pleasure for me to thank again to Aj. Chinorat and Aj. Yan for their kindness and for financial support during my study at SUT.

Ayut Limphirat

CONTENTS

	Page
ABSTRACT IN THAI	I
ABSTRACT IN ENGLISH	II
ACKNOWLEDGEMENTS	IV
CONTENTS	V
LIST OF TABLES	VIII
LIST OF FIGURES	X
CHAPTER	
I INTRODUCTION	1
1.1 Review of hypernucleus	2
1.2 Experiments proposed by Pochodzalla	5
1.3 The FAIR project	7
1.4 Review of transport models	10
1.5 Research objectives	12
1.6 Scope and limitations of the study	13
II THE UrQMD MODEL	14
2.1 Initialization	15
2.2 Equations of motion	16
2.3 Cross sections	21
2.3.1 Baryon-antibaryon	22
2.3.2 Baryon-baryon	26
2.3.3 The additive quark model	26

CONTENTS (Continued)

	Page
2.4 Reaction channels	27
2.4.1 Resonances	28
2.4.2 Strings	28
 III STRANGE PARTICLE AND NON-STRANGE PARTICLE	
PRODUCTION	34
3.1 UrQMD results on strange particle production	35
3.2 UrQMD results on non-strange particle production	40
3.3 Model predictions for $\Xi\bar{\Xi}$ production	41
 IV HYPERNUCLEUS PRODUCTION	
4.1 Experimental trigger conditions	44
4.2 Deceleration mechanism	47
4.3 Hyperon induced reactions	48
 V SUMMARY	
 APPENDICES	
APPENDIX A THE FAIR FACILITIES	62
APPENDIX B LORENTZ TRANSFORMATION	64
APPENDIX C KINEMATIC VARIABLES	66
APPENDIX D TWO-BODY ELASTIC SCATTERING	69
APPENDIX E THERMAL DISTRIBUTION	72
APPENDIX F DATA ANALYSIS SCRIPT	81
F.1 Multiplicity analysis script	81
F.2 Transverse momentum analysis script	83
F.3 Rapidity analysis script	86

CONTENTS (Continued)

	Page
F.4 Analysis script for read the data of Ξ^-	89
F.5 Scattering number analysis script	91
F.6 Momentum distribution analysis script	93
APPENDIX G PUBLICATION PAPER	96
CURRICULUM VITAE	103

LIST OF TABLES

Table		Page
1.1	Comparison of hypernucleus ${}^4_{\Lambda}\text{H}$ production rates obtained by the KEK at Japan (Tamura et al., 1989) and the European K^- collaboration (Davis, 1991).	3
1.2	Rates of hypernucleus ${}^3_{\Lambda}\text{H}$ and ${}^5_{\Lambda}\text{H}$ productions obtained by the European K^- collaboration (Davis, 1991).	4
2.1	Parameters of the hard equation of state implemented in the UrQMD model, with and without Pauli-potential.	20
2.2	Baryons and baryon-resonances included into the UrQMD model. Through baryon-antibaryon symmetry the respective antibaryon states are included as well.	22
2.3	Mesons and meson-resonances, sorted with respect to spin and parity, included into the UrQMD model.	23
2.4	Parameters for the CERN/HERA parameterization for the total and elastic antiproton -proton cross-sections. This parameterization is used in UrQMD for momenta $p_{lab} > 5\text{GeV}/c$	25
2.5	Masses (GeV/c^2), widths (MeV) and branching ratios of non-strange baryon-resonances in UrQMD. All parameters are within the range given by the Review of Particle Properties (Barnett et al., 1996a).	29

LIST OF TABLES (Continued)

Table		Page
2.6	Masses (GeV/c^2), widths (MeV) and branching ratios of single-strange baryon-resonances in UrQMD. All parameters are within the range given by the Review of Particle Properties (Barnett et al., 1996a).	30
2.7	Masses (GeV/c^2), widths (MeV) and branching ratios of double-strange baryon-resonances in UrQMD. All parameters are within the range given by the Review of Particle Properties (Barnett et al., 1996a).	31
2.8	Probabilities for the different meson-multiplets in the UrQMD model.	32
3.1	Comparison between experimental data (Grigalashvili et al., 1999) and UrQMD results for the average multiplicities of $\Lambda(\Sigma^0)$ and $\bar{\Lambda}(\bar{\Sigma}^0)$	36
3.2	Comparison between experimental data by the NA5 collaboration (Derado et al., 1991) and UrQMD results on average multiplicities of Λ , K^0 , negative hadrons (h^-) and ratios.	38

LIST OF FIGURES

Figure	Page
1.1	Steps of the proposed reaction in the case of double hypernucleus production. 6
1.2	The existing GSI facility (blue) and the new FAIR facility (red) (GSI, 2001). 9
1.3	Layout of the antiproton beam (orange dashed line) production by proton beam (orange line) collide with the nuclear target (GSI, 2001). 10
2.1	The $\bar{p}p$ cross-section as compared to the experimental data (Barnett et al., 1996a) on total (open circles), elastic (open squares), and annihilation (open triangles) cross-sections. The diffractive cross-section is assumed to be a difference between the total cross-section and the sum of the elastic and annihilation cross-section. 24
2.2	Particle production in a string. 32
3.1	Layout of experiment at Serpukhov proton synchrotron (Boos et al., 1984). 36
3.2	Layout of NA5 experiment at CERN SPS (De Marzo et al., 1982). 37
3.3	UrQMD results compared with experimental data (Derado et al., 1991) for transverse momentum distributions (upper panels) and normalized laboratory rapidity distributions (lower panels). Here the Λ (left panels) and the K^0 (right panels) are produced in $\bar{p} + \text{Xe}$ reaction at 200 GeV. 39

LIST OF FIGURES (Continued)

Figure		Page
3.4	Layout of Fermilab 30-inch bubble chamber spectrometer and downstream particle identifier (Whitmore et al., 1994).	41
3.5	UrQMD results compared with experimental data (Whitmore et al., 1994) for p_t^2 distributions of π^- (left panels) and π^+ (right panels) produced in $\bar{p} + \text{Mg}$, Ag and Au at a \bar{p} momentum of 100 GeV/c.	42
3.6	Multiplicities of Ξ^- and $\bar{\Xi}^+$ from the reactions of $\bar{p} + \text{Mg}$, Cu and Au collisions.	43
4.1	Multiplicity comparison between the Ξ , $\bar{\Xi}$ and the K^+K^+ pair in $\bar{p}+\text{Au}$ reactions at center of mass energies from 3 to 4 GeV. The solid square, solid circle, open triangle and open diamond symbols indicate respectively the multiplicities of Ξ^- , Ξ^0 , $\bar{\Xi}^+$ and $\bar{\Xi}^0$ while the open squares denote the multiplicity of K^+K^+ pair.	46
4.2	Momentum distribution of K^+ (from K^+K^+ pair) in $\bar{p}+\text{Au}$ reactions at $\sqrt{s} = 4$ GeV.	47
4.3	\sqrt{s} distribution of the antibaryon-baryon interactions that lead to the production of a Ξ^- baryon in $\bar{p}+\text{Au}$ reactions at $\sqrt{s} = 4$ GeV. Square and circle symbols denote the \sqrt{s} distributions of the $\bar{p}+p \rightarrow \Xi^- + \bar{\Xi}^+ + \text{X}$ channel and the $\bar{p}+n \rightarrow \Xi^- + \bar{\Xi}^0 + \text{X}$ channel, respectively.	48
4.4	Distribution of the number of scatterings (Nos) of the produced Ξ s in $\bar{p}+\text{Au}$ reactions at $\sqrt{s} = 4$ GeV.	49

LIST OF FIGURES (Continued)

Figure		Page
4.5	Comparison of momentum spectra of the Ξ^- between $\bar{p} + p$ and $\bar{p} + \text{Au}$ reactions at $\sqrt{s} = 4$ GeV. Square symbols denote the data from $\bar{p} + \text{Au}$ reaction, while circle symbols show the data from $\bar{p} + p$ reaction. Here, the momenta are given in the target frame.	50
4.6	Momentum spectra of Ξ^- in $\Xi^- + \text{Au}$ reactions inside the secondary target at laboratory momenta from 10 to 800 MeV/c.	52
D.1	Two-body scattering.	70
E.1	Limit of $z^2 K_2(z)$ when $z \rightarrow 0$	77

CHAPTER I

INTRODUCTION

A major topic in today's astrophysics is to understand the composition of neutron stars. Over the last years, it became clear that neutron stars might have a complicated structure with different phases ranging from pure quark matter to hyperon (a type of baryon which consists of one or more strange quark) matter and dense baryonic matter. Thus, hyperons are likely to be present in neutron stars in addition to nucleons and one has to consider the interactions between all (strange and non-strange) baryons. Experimental nuclear astrophysics offers unique possibilities to explore these questions as it allows to explore the equation of state of dense baryonic matter and (multi-)strange baryonic matter.

There are some information from hypernuclear physics of the interactions between hyperons (Y) and nucleons (N), but the understanding of the interactions between hyperons themselves is really scarce (Dover et al., 1989). The hyperon-hyperon (YY) interaction is not really well known, there are just a few double Λ hypernuclear events (Aoki et al., 1991; Ahn et al., 2001; Takahashi et al., 2001; Gal, 2005). The interaction between other pairs of hyperons as $\Lambda\Xi$ or $\Xi\Xi$ is not known at all experimentally. However, the hyperon-hyperon interactions are essential for the determination of the composition of neutron star matter, so basic hypernuclear data can provide substantial input for the modeling of neutron star matter. The planned PANDA (Proton ANtiproton at DArmstadt) experiment (Kotulla et al., 2004) at the currently build Facility for Anti-proton and Ion Research (FAIR) near GSI (Gesellschaft für SchwerIonenforschung), Darmstadt will be able to explore

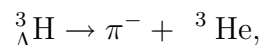
the formation and properties of $\Lambda\Lambda$ hypernuclear systems (Pochodzalla, 2005), which will be used to provide the important information for $\Lambda\Lambda$ interaction as well as the neutron star.

Given in this chapter are the overview of hypernucleus, experimental purposes, the FAIR project and transport models, and the objectives and scope of this study.

1.1 Review of hypernucleus

A hypernucleus is a nucleus which contains at least one hyperon in addition to nucleons, or one can say that, it is a nucleus which an up (u) or down (d) quark is replaced by a strange (s) quark. That means the strangeness quantum number is involved in the nucleus. This kind of nucleus offers a variety of new and exciting perspectives in nuclear spectroscopy and for studying the forces among hyperons and nucleons. Also it is expected to provide new insights into the properties of neutron stars.

The hypernucleus was first proposed in October 1952 by Polish physicists Marion Danysz and Jerzy Pniewski (Danysz and Pniewski, 1953). It has been observed in a high energy interactions between cosmic ray and a heavy emulsion nucleus which emits a multiply charged fragment. Then a very similar event had been found at Imperial College London (Tidman et al., 1953). In 1954 the first complete event was found as the process of



and was confirmed that the bound particle was a Λ hyperon (Bonetti et al., 1954).

Later the productions of hypernucleus were measured by several ways, for example, by accelerating the proton and pion beams. With these ways the rate

Table 1.1 Comparison of hypernucleus ${}^4_{\Lambda}\text{H}$ production rates obtained by the KEK at Japan (Tamura et al., 1989) and the European K^- collaboration (Davis, 1991).

KEK at Japan		European K^- collaboration	
Target	Rate ($\times 10^{-3}$)	Target	Rate ($\times 10^{-3}$)
${}^7\text{Li}$	30		
${}^9\text{Be}$	15.7		
${}^{12}\text{C}$	10.0	C, N, O	7.3
${}^{16}\text{O}$	4.7		
${}^{40}\text{Ca}$	<2.7	Ag, Br	2.4

of hypernucleus productions were low and too much background were occurred. In the late of 1950s the separated beam of K^- was used to obtains the copious of hypernucleus production with little background. The properties of lightest hypernucleus were studied at this time by stopping K^- mesons in a helium bubble chamber.

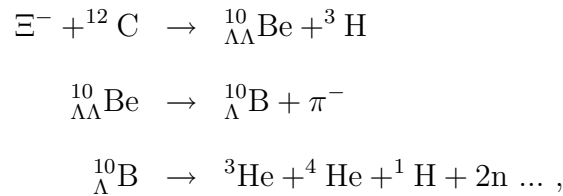
Review of hypernucleus ${}^4_{\Lambda}\text{H}$ production rates, by stopping K^- mesons, are shown as Table 1.1. In this table, the production rates obtained by the KEK at Japan (Tamura et al., 1989) are compared with the European K^- collaboration (Davis, 1991). Table 1.2 depicts the rates of hypernucleus ${}^3_{\Lambda}\text{H}$ and ${}^5_{\Lambda}\text{H}$ productions obtained by the European K^- collaboration (Davis, 1991).

In 1963 the double hypernucleus, ${}^{10}_{\Lambda\Lambda}\text{Be}$, was first discovered by Danysz and Pniewski (Danysz et al., 1963a; Danysz et al., 1963b). Three years later, the ${}^6_{\Lambda\Lambda}\text{He}$ was indirectly observed and reported in (Prowse, 1966). The production of $\Lambda\Lambda$ hypernucleus were still ambiguous until the first directly observation in year 1991 by the physicists at KEK (High Energy Accelerator Research Organization),

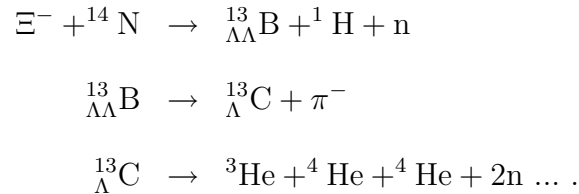
Table 1.2 Rates of hypernucleus ${}^3_{\Lambda}\text{H}$ and ${}^5_{\Lambda}\text{H}$ productions obtained by the European K^- collaboration (Davis, 1991).

Target	${}^3_{\Lambda}\text{H}$ rate ($\times 10^{-3}$)	${}^5_{\Lambda}\text{H}$ rate ($\times 10^{-3}$)
C, N, O	1.62	21.6
Ag, Br	0.54	1.4

Tsukuba, Japan (Aoki et al., 1991). They observed the ${}^{10}_{\Lambda\Lambda}\text{Be}$ and ${}^{13}_{\Lambda\Lambda}\text{B}$ from the reactions:

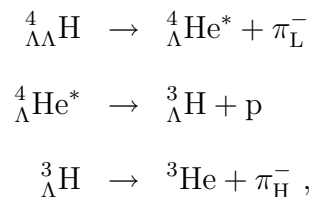


and



Note that the Ξ^- s were produced from the (K^-, K^+) reactions.

Recently, another kind of $\Lambda\Lambda$ hypernucleus, ${}^4_{\Lambda\Lambda}\text{H}$, were observed by the experiment E906 at Brookhaven-AGS (alternating gradient synchrotron), USA (Ahn et al., 2001). Within this experiment the produced hypernucleus was decayed by the processes:



where the π_L^- and π_H^- are the pions with lower momentum and higher momentum respectively. These two pions are the important key for the measurement technique because each pion associated with one unit of strangeness change.

Moreover the next example of $\Lambda\Lambda$ hypernucleus is ${}^6_{\Lambda\Lambda}\text{He}$ reported by the experiment E373 at KEK (Takahashi et al., 2001). The experiment has been performed by using the K^- beam of 1.66 GeV/c collides with the diamond target in order to produce the Ξ^- particles. Then the ${}^6_{\Lambda\Lambda}\text{He}$ is created from the reaction:



where ${}^6_{\Lambda\Lambda}\text{He} \rightarrow {}^5_{\Lambda}\text{He} + \text{p} + \pi^-$.

Up to now the world experimental data on $\Lambda\Lambda$ hypernucleus is very limited. Its observation were also reported with low statistics. To gain new insights, the study of $\Lambda\Lambda$ hypernucleus is one of the research directions which will be explored at the Facility for Antiproton and Ion Research (FAIR) with the PANDA experiment. Next section the experimental purpose, which will be used to explore the production of $\Lambda\Lambda$ hypernucleus, is reviewed.

1.2 Experiments proposed by Pochodzalla

In this section we review an idea proposed by Pochodzalla to use anti-proton induced reactions in order to obtain a beam of Ξ s or Ω s which are then directed at a secondary target to produce a multi-hyper-nucleus, see Fig. 1.1 for a schematical illustration. The high energy storage ring (HESR), one of the major components of the proposed international facility at FAIR (GSI), will provide antiprotons with high luminosity which have momenta between 1.5 and 15 GeV/c and are phase space cooled (GSI, 2001). At the HESR facility the detector PANDA (Proton ANTiproton at DArmstadt) is expected to concentrate amongst others on high

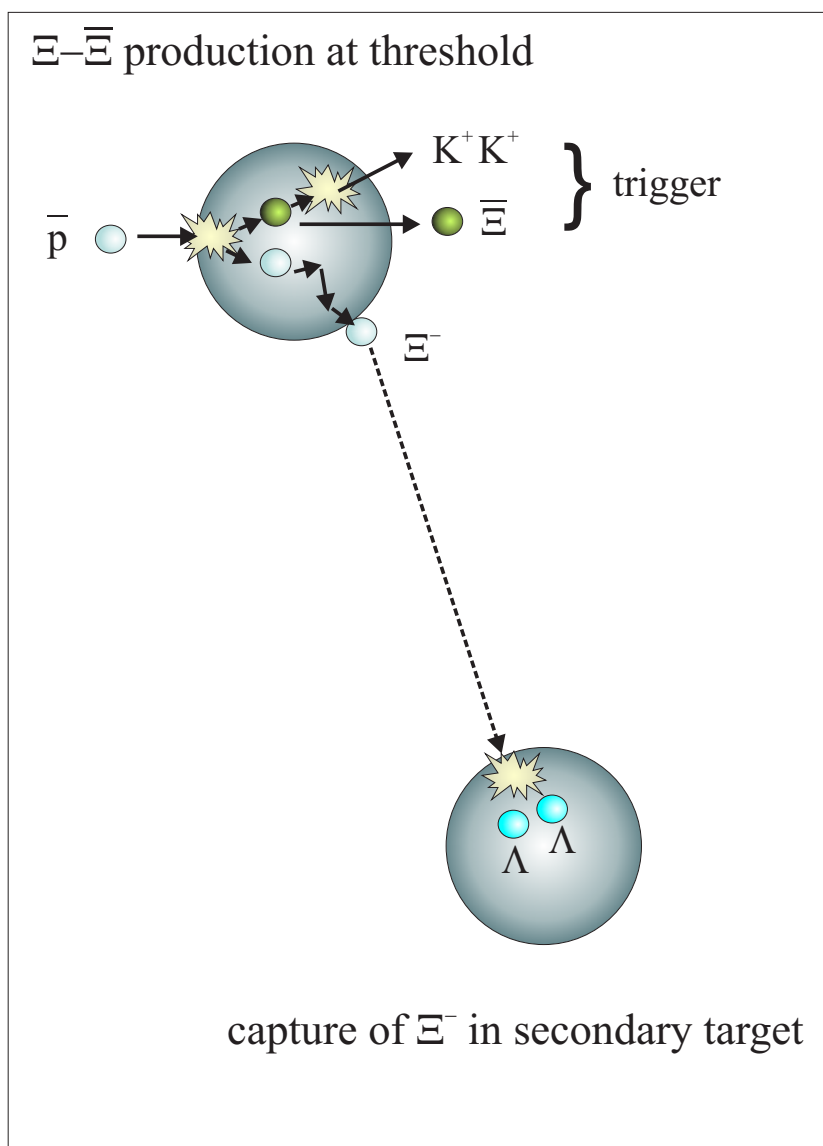


Figure 1.1 Steps of the proposed reaction in the case of double hypernucleus production.

resolution spectroscopy of double hypernuclei. In order to take into account a wide range of energies together with a full angular coverage with high resolution, this proposed detector combines two spectrometers: a target spectrometer and a forward dipole spectrometer. It is sufficiently flexible to be used for different experimental purposes, e.g., experiments with strange double-hypernuclei and Ω -atoms. Details concerning the tracking and identification of the produced particles have

been discussed in Ref. (Pochodzalla, 2005). The production of hypernuclei and hyperatoms at HESR will use $\Xi\bar{\Xi}$ and $\Omega\bar{\Omega}$ pair production close to threshold in antiproton nucleus collisions in order to minimize the background from associated particles. The trigger will be based on the detection of high momentum antihyperons at small angles or of positive kaons produced by the antihyperons absorbed in a primary target nucleus. In the second step of the experiment, the Ξ (Ω) inside this nucleus are decelerated and subsequently absorbed in a secondary active target whose geometry is determined by the short mean life time of the Ξ of only 0.164 ns. The distance between the primary and the secondary target (absorber) has to be chosen in the right manner to guarantee that Ξ s (and Ω s) with low and high momenta are fully stopped in the absorber before they decay. In order to track the stopped Ξ and the charged fragments resulting from the decay of the produced hypernuclei, it is planned to sandwich the absorber with solid state pixel or strip detectors. In combination with an efficient germanium array, the novel solid-state tracking system proposed by Pochodzalla (Pochodzalla, 2005) together with the high luminosity beam of antiprotons from the planned HESR opens the opportunity for high resolution γ -spectroscopy of $\Lambda\Lambda$ -hypernuclei and Ω -atoms at the PANDA experiment of the future international accelerator facility at FAIR (GSI). The overview of the FAIR project will be shown in the next section.

1.3 The FAIR project

The FAIR project is a new international research facility at GSI which located in Darmstadt, Germany. There are 14 states of partner involved in this project. The estimated total cost of the facility is 675 Million Euro. The principle goal of the project is to perform future forefront research in the sciences concerned with the basic structure of matter, and in intersections with other fields. It can

be described by the following widely objectives (GSI, 2001):

- investigations with beams of short-lived radioactive nuclei, addressing important questions concerning nuclei far from stability, areas of astrophysics and nucleosynthesis in supernovae and other stellar processes, and tests of fundamental symmetries,
- the study of hadronic matter at the sub-nuclear level with beams of antiprotons, in particular of the following two key aspects: confinement of quarks and the generation of the hadron masses, the latter being intimately connected to the spontaneous breaking of chiral symmetry, a fundamental property of strong interactions,
- the study of compressed, dense hadronic matter through nucleus-nucleus collisions at high energies,
- the study of bulk matter in the high-density plasma state, a state of matter of interest for inertial confinement fusion and various astrophysical settings,
- studies of Quantum Electrodynamics (QED), of extremely strong (electromagnetic) field effects, and of ion-matter interactions.

To satisfy these goals, the FAIR will provide the high intensity and high quality of both primary and secondary beams. These include beams of short-lived (radioactive) nuclei and beams of antiprotons.

An illustration of the exiting GSI facility and the new FAIR facility is shown in Fig. 1.2. Blue is represented for the exiting GSI facility including the linear accelerator UNILAC, the heavy-ion synchrotron SIS18 and the experiment storage ring (ESR). The new FAIR facility is illustrated by red color involving the double-ring synchrotron SIS100/200, the high-energy storage ring (HESR), the collector

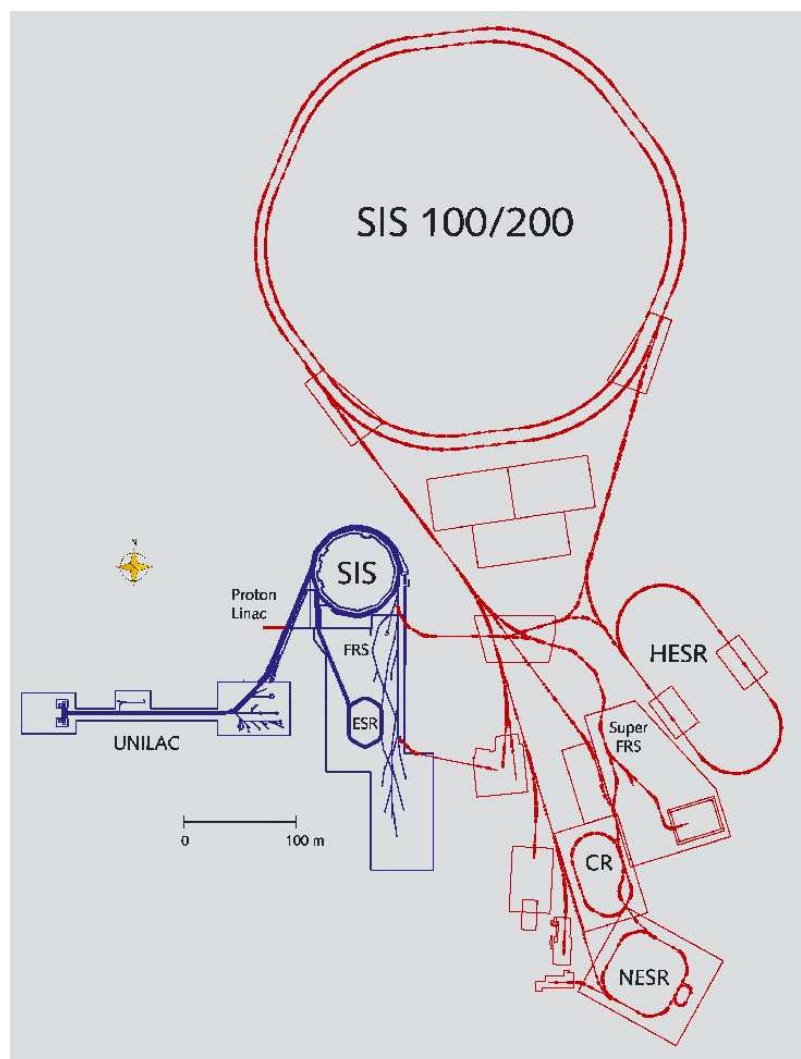


Figure 1.2 The existing GSI facility (blue) and the new FAIR facility (red) (GSI, 2001).

ring (CR), the new experiment storage ring (NESR) and the super-conducting fragment separator (Super-FRS). One can see in appendix A for more details.

The productions of $\Lambda\Lambda$ hypernucleus will be investigated in the PANDA at the HESR by antiproton-nucleus collisions. Here the process for antiproton beam production is illustrated in Fig. 1.3. As seen in this figure the 50 MeV proton beam (orange line) from proton linac can be accelerated with energy up to 2 GeV at the SIS18 then injected into the SIS100. At SIS100 the proton beam can be

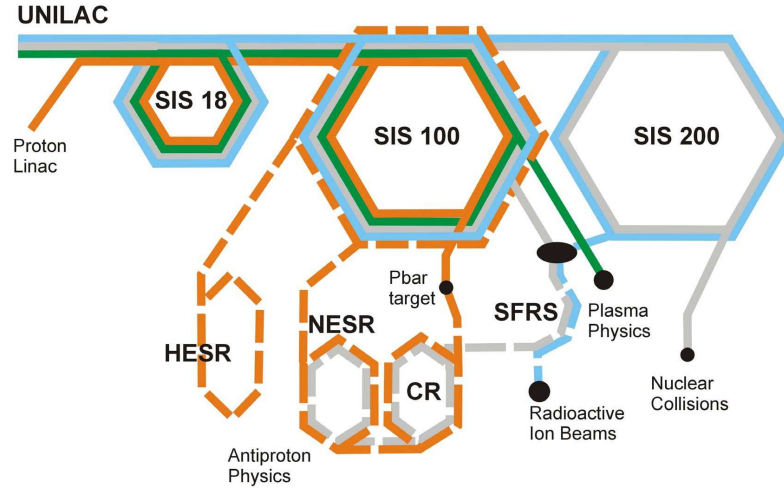


Figure 1.3 Layout of the antiproton beam (orange dashed line) production by proton beam (orange line) collide with the nuclear target (GSI, 2001).

accelerated up to the energy of 29 GeV then collide with nuclear target in order to produce antiproton beam (orange dashed line). Next the produced antiproton beam will be accumulated in CR/NESR. Later the accumulated antiproton in the NESR will be transferred to the SIS100, to be accelerated up to 14 GeV. Finally it will be injected into a HESR, to perform experiments with an internal target.

1.4 Review of transport models

As mention above, the study of $\bar{p}+A$ collision give many important result in hypernucleus studies. To understand each process, we use theoretical model to explain the collision. There are many kind of model before Ultrarelativistic Quantum Molecular Dynamics model (UrQMD) (Bass, Belkacem, Bleicher et al., 1998). Here, we would like to give a short review of some important model such as Boltzmann Uehling Uhlenbeck model (BUU), Vlasov Uehling Uhlenbeck model (VUU) (Aichelin, Peilert, Bohnet, Rosenhauer, Stoecker and Griner, 1998; Kruse, Jacak, Molitoris, Westfall and Stoecker, 1985) and others.

In the early 1933, E.A. Uhling and G.E. Uhlenbeck used Uhling Uhlenbeck equation (Uhling and Uhlenbeck, 1933) to study nuclear collisions. Later, BUU model (Aichelin, Peilert, Bohnet, Rosenhauer, Stoecker and Griner, 1998) was used in studying the evidence of heavy ion collision and considered the production of medium mass cluster with atomic number between 5 and 30 and the incident particle energy more than 25 MeV/nucleon. But the results from BUU model do not fit with the exact data because it used only classical potential.

In 1985, Vlasov had developed the VUU model (Kruse, Jacak, Molitoris, Westfall and Stoecker, 1985) which had the same objective as BUU model with the attempt to describe each particles after collisions and consider potential in the form of mean field potential. However, the mean field potential is not completed since it does not cover the effect of many body collisions. Therefore the results from VUU model can not match the experimental data.

Another approach to study the collision is by using microscopic model such as Time Dependent Hartree-Fock (TDHF) (Bonche, Koonin and Negele, 1976), Classical Molecular Dynamics model (CMD) (Bodmer and Panos, 1977) and Quantum Molecular Dynamics model (QMD) (Aichelin, 1991). Time Dependent Hartree-Fock (Bonche, Koonin and Negele, 1976) is suggested by Dirac using the idea of explaining the collisions in term of parameter density and temperature.

Next, Classical Molecular Dynamics model (CMD) (Bodmer and Panos, 1977) is another microscopic model which can be used to find cross-section. To obtain the cross-section in CMD, it is necessary to know interaction force between 2 nucleon and many value such as momentum which can be calculated from equation of motion of incident nucleon. However, the CMD can not give exact data if the energy of particle is greater than 100 MeV. To improve the CMD model we move onto quantum mechanics by representing each nucleon by Gaussian wave function

and considering the interaction only two and three particle. This new model is called Quantum Molecular Dynamics model (QMD) (Aichelin, 1991). The validity of this model is in the intermediate energy between 100 MeV to 2 GeV.

If the energy is higher than 2 GeV, we have to include relativistic effect into the model. The model is now become Ultrarelativistic Quantum Molecular Dynamics model (UrQMD) (Bass, Belkacem, Bleicher et al., 1998; Bleicher et al., 1999).

Again, we will give briefly details of the measurements which are done at heavy ion facilities in three energy regimes: i) energy about 1 AGeV at BEVALAC in Berkeley, USA or SchwerIonenSynchrotron (SIS) at GSI-Darmstadt, Germany; ii) energy about 2-15 AGeV at the Alternating Gradient Synchrotron (AGS), in Brookhaven; iii) at the Super Proton Synchrotron (SPS) in CERN, energy about 40-200 AGeV. In the future, much higher energies will be available at the Relativistic Heavy Ion Collider (RHIC) in Brookhaven ($\sqrt{s} \approx 200$ AGeV) and the Large Hardron Collider (LHC) in CERN ($\sqrt{s} \approx 6$ ATeV).

1.5 Research objectives

1. To examine the threshold energy of $\Xi\bar{\Xi}$ productions.
2. To find out the properties of triggers.
3. To study the deceleration mechanism of Ξ inside the primary nucleus.
4. To study the capture of Ξ in the secondary nucleus.

1.6 Scope and limitations of the study

We study antiproton-nucleus ($\bar{p}+A$) collisions in the ultrarelativistic quantum molecular dynamics model to find out the $\Xi\bar{\Xi}$ productions and their properties. The collision energies are close to the threshold energy of $\Xi\bar{\Xi}$ productions. We also compare our theoretical results with experimental data.

This thesis is structured as follows: Chapter II gives a description of the UrQMD model which is used in this work. In the Chapter III shows the results of antiproton-nucleus collisions for strange and non-strange particle production which are compared with the experimental data. Chapter IV depicts the predictions on the double Λ hypernucleus productions. The last chapter (Chapter V) gives our conclusions.

CHAPTER II

THE UrQMD MODEL

As mentioned before, the Ultra-relativistic Quantum Molecular Dynamics (UrQMD) model will be used in this work. This model has been developed over ten years by hundreds of physicists since it was initiated by Frankfurt Heavy-Ion Group, Institute for Theoretical Physics, Frankfurt University. The main goals are to gain understandings, within a single transport model, of the following physical phenomena such as: creation of dense hadronic matter at high temperatures; properties of nuclear matter, delta and resonance matter; creation of mesonic matter and of anti-matter; creation and transport of rare particles in hadronic matter; creation, modification and destruction of strangeness in matter; emission of electromagnetic probes. The model describes the relativistic heavy ion collisions in the energy range from AGS (Alternating Gradient Synchrotron, Brookhaven) up to SPS (Super Proton Synchrotron, CERN) and RHIC (Relativistic Heavy Ion Collider, Brookhaven).

In this chapter, we begin by describing the projectile and target nuclei of the collisions defined by the UrQMD model. Then in section 2.2 we explain the potentials used in this model. Finally, at the end of this chapter we present 55 baryon species, 32 meson species, the cross section of $\bar{p}p$ collisions and the string model which will be used later in chapter III.

2.1 Initialization

In the UrQMD model (Bass et al., 1998; Bleicher et al., 1999; Petersen et al., 2008), the nucleon are expressed in term of Gaussian shaped density distributions,

$$\varphi_j(\vec{x}_j, t) = \left(\frac{2\alpha}{\pi}\right)^{\frac{3}{4}} \exp \left\{ -\alpha \left(\vec{x}_j - \vec{r}_j(t)\right)^2 + \frac{i}{\hbar} \vec{p}_j(t) \cdot \vec{x}_j \right\} \quad (2.1)$$

and the wave function of the nucleus are written in term of the product wave function of the single nucleon Gaussian

$$\Phi = \prod_j \varphi_j(\vec{x}_j, \vec{p}_j, t). \quad (2.2)$$

Each initialized nucleus must satisfy the following conditions:

- $\sum_i \vec{q}_i = 0$, i.e., it is concentrated in configuration space around 0
- $\sum_i \vec{v}_i = 0$, i.e., the nucleus is at rest
- its binding energy should agree with the value given by the Bethe-Weizsacker formula,
- the radius should depend on mass number

$$R(A) = r_0 \left[\frac{1}{2} \left\{ A + \left(A^{\frac{1}{3}} - 1 \right)^3 \right\} \right]^{\frac{1}{3}} \quad (2.3)$$

and have a suitable surface-thickness,

- in its center, the nucleus should have nuclear matter ground state density.

The radius r_0 is defined in term of a function of the nuclear matter ground state density (ρ_0) which is used in the UrQMD model:

$$r_0 = \left(\frac{3}{4\pi\rho_0} \right)^{\frac{1}{3}}. \quad (2.4)$$

The initial momenta of the nucleons are randomly chosen from 0 to the local Thomas-Fermi-momentum,

$$p_F^{\max} = \hbar c (3\pi^2 \rho)^{\frac{1}{3}} \quad (2.5)$$

where ρ is local proton density.

The interactions include non-relativistic density-dependent Skyrme potential with additional Yukawa and Coulomb potentials. Momentum dependent potentials are not used, while Pauli-potential, may be included optionally.

2.2 Equations of motion

In this section the potential and kinetic terms which are important parts in Hamiltonion are introduced. First, the potential parts are the Skyrme, Yukawa, Coulomb and Pauli potential. Then in the second part, the complete Hamiltonion of UrQMD is given. Eq. (2.1) gives the nucleon- or baryon-density,

$$\rho_j(\vec{x}_j, t) = \left(\frac{2\alpha}{\pi}\right)^{\frac{3}{2}} \exp\left\{-2\alpha\left(\vec{x}_j - \vec{r}_j(t)\right)^2\right\} \quad (2.6)$$

where \vec{x}_j and $\vec{r}_j(t)$ are the quantum mechanical position variable and the classical parameter of the Gaussian respectively. The Skyrme-Potential (momentum-dependence and spin-exchange has been neglected) is

$$V^{Sk} = \frac{1}{2!} t_1 \sum_{j,k} \delta(\vec{x}_i - \vec{x}_k) + \frac{1}{3!} t_2 \sum_{j,k,l} \delta(\vec{x}_j - \vec{x}_k) \delta(\vec{x}_j - \vec{x}_l) \quad (2.7)$$

where in order to exclude self-interactions, all terms where at least two indices are identical, are discarded in the prime sum. This potential composes of a sum of two- and a three-body interaction terms. The first term, which is the two-body term, is responsible for the long range attractive component of the nucleon-nucleon interaction and the second term is responsible for the short range repulsive part

of the interaction. The two-body Skyrme potential of particle j is obtained by putting Eq. (2.1) into the first term of Eq. (2.7),

$$\begin{aligned} V_j^{Sk2} &= \sum_k^N \int d\vec{x}_j d\vec{x}_k \varphi_j^* (\vec{x}_j) \varphi_k^* (\vec{x}_k) t_1 \delta (\vec{x}_j - \vec{x}_k) \varphi_j (\vec{x}_j) \varphi_k (\vec{x}_k), \\ V_j^{Sk2} &= t_1 \sum_k^N \left(\frac{\alpha}{\pi} \right)^{\frac{3}{2}} \exp \left\{ -\alpha (\vec{r}_j - \vec{r}_k)^2 \right\}, \\ V_j^{Sk2} &= t_1 \rho_j^{\text{int}} (\vec{r}_j). \end{aligned} \quad (2.8)$$

In the last line of Eq. (2.8), the interaction density was introduced. It has the same form as nucleon density (2.6) which is obtained from the Wigner-transform of the Gaussian (2.1), but omits the nucleon at the location j and its Gaussian has twice the width of that used in equation (2.6). The three-body potential for particle j can be obtained in the same way as Eq. (2.8)

$$\begin{aligned} V_j^{Sk3} &= \frac{1}{2!} \sum_{kl}^N \int d\vec{x}_j d\vec{x}_k d\vec{x}_l \varphi_j^* (\vec{x}_j) \varphi_k^* (\vec{x}_k) \varphi_l^* (\vec{x}_l) \\ &\quad \times t_2 \delta (\vec{x}_j - \vec{x}_k) \delta (\vec{x}_j - \vec{x}_l) \varphi_j (\vec{x}_j) \varphi_k (\vec{x}_k) \varphi_l (\vec{x}_l) \\ V_j^{Sk3} &= t_2 \frac{1}{2!} \sum_{kl}^N \left(\frac{4\alpha^2}{3\pi^2} \right)^{\frac{3}{2}} \\ &\quad \times \exp \left\{ -\frac{2}{3} \alpha \left((\vec{r}_j - \vec{r}_k)^2 + (\vec{r}_k - \vec{r}_l)^2 + (\vec{r}_l - \vec{r}_j)^2 \right) \right\}. \end{aligned} \quad (2.9)$$

From the Eq. (2.9), if we considered the infinite nuclear matter case, the individual relative distances should approximately equal to their average value. Therefore, the relative distance of particle k and l may be replaced by the average of the other two relative distances

$$V_j^{Sk3} \approx t_2 \frac{1}{2!} \sum_{kl}^N \left(\frac{4\alpha^2}{3\pi^2} \right)^{\frac{3}{2}} \exp \left\{ -\alpha \left((\vec{r}_j - \vec{r}_k)^2 + (\vec{r}_l - \vec{r}_j)^2 \right) \right\}. \quad (2.10)$$

Eq. (2.10) can be rewritten as Eq. (2.11) using the definition of interaction density from Eq. (2.8).

$$V_j^{Sk3} \approx t_2 3^{-\frac{3}{2}} (\rho_j^{\text{int}})^2. \quad (2.11)$$

The differences between Eq. (2.8) and (2.11) are the coefficient and the power of the interaction density term,

$$V_j^{Sk3} \approx t_\gamma (\gamma + 1)^{-\frac{3}{2}} (\rho_j^{\text{int}})^\gamma. \quad (2.12)$$

Expression (2.12) is a generalized form of the three body interaction. It is always used in the UrQMD model. When $\gamma=2$, the equation above turns to the interaction of three body term.

The Yukawa, Coulomb, and (optional) Pauli potentials can be written in term of two-body interactions which are shown in Eq. (2.13), (2.14) and (2.15), respectively.

$$V_{Yuk}^{ij} = V_0^{Yuk} \frac{\exp \left\{ - \frac{|\vec{r}_i - \vec{r}_j|}{\gamma_Y} \right\}}{|\vec{r}_i - \vec{r}_j|} \quad (2.13)$$

$$V_{Coul}^{ij} = \frac{Z_i Z_j e^2}{|\vec{r}_i - \vec{r}_j|} \quad (2.14)$$

$$V_{Pau}^{ij} = V_{Pau}^0 \left(\frac{\hbar}{q_0 p_0} \right)^3 \exp \left\{ - \frac{|\vec{r}_i - \vec{r}_j|^2}{2q_0^2} - \frac{|\vec{p}_i - \vec{p}_j|^2}{2p_0^2} \right\} \delta_{\tau_i \tau_j} \delta_{\sigma_i \sigma_j} \quad (2.15)$$

where γ_Y is a parameter given in Table (2.1), Z_j represents its charge, τ_j is isospin and σ_j is the spin of particle j .

For the infinite nuclear matter, the contribution of the Yukawa-potential for the total energy has the same linear density-dependence as the two-body Skyrme-contribution. As a result all parameter sets which satisfy the following relation for the parameter t_1 yield the same equation of state in infinite nuclear matter

$$\frac{1}{2} t_1 + 2\pi V_0^{Yuk} \gamma_Y^2 = \text{const.} \quad (2.16)$$

For finite nuclei, the parameter of Yukawa potential are the same without changing the equation of state.

Finally, we get the classical UrQMD Hamiltonian which covers the motion of the parameters, \vec{r}_j and \vec{p}_j , of the wave-functions as

$$H_{UrQMD} = \sum_{j=1}^N E_j^{kin} + \frac{1}{2} \sum_{j=1}^N \sum_{k=1}^N (E_{jk}^{Sk2} + E_{jk}^{Yukawa} + E_{jk}^{Coulomb} + E_{jk}^{Pauli}) + \frac{1}{6} \sum_{j=1}^N \sum_{k=1}^N \sum_{l=1}^N E_{jkl}^{Sk3} \quad (2.17)$$

where the kinetics term is

$$E_j^{kin} = \sqrt{p_j^2 + m_j^2} \quad (2.18)$$

and the two body Skyrme is

$$E_{jk}^{Sk2} = t_1 \left(\frac{\alpha}{\pi} \right)^{\frac{3}{2}} \exp \{ -\alpha r_{jk}^2 \} \quad (2.19)$$

and the three body Skyrme is

$$E_{jkl}^{Sk3} = t_\gamma \left(\frac{4\alpha^2}{3\pi^2} \right)^{\frac{3}{2}} \exp \{ -\alpha (r_{jk}^2 + r_{jl}^2) \}. \quad (2.20)$$

The Yukawa potential is

$$E_{jk}^{Yukawa} = V_0^{Yuk} \frac{1}{2r_{jk}} \exp \left\{ \frac{1}{4\alpha\gamma_Y^2} \right\} \times \left[\exp \left\{ -\frac{r_{jk}}{\gamma_Y} \right\} \left(1 - \text{erf} \left(\frac{1}{2\gamma_Y\sqrt{\alpha}} - \sqrt{\alpha}r_{jk} \right) \right) - \exp \left\{ \frac{r_{jk}}{\gamma_Y} \right\} \left(1 - \text{erf} \left(\frac{1}{2\gamma_Y\sqrt{\alpha}} + \sqrt{\alpha}r_{jk} \right) \right) \right] \quad (2.21)$$

and the Coulomb potential is

$$E_{jk}^{Coulomb} = \frac{Z_i Z_j e^2}{r_{jk}} \text{erf}(\sqrt{\alpha}r_{jk}) \quad (2.22)$$

and the Pauli potential is

$$E_{jk}^{Pauli} = V_{Pau}^0 \left(\frac{\hbar}{p_0 q_0} \right)^3 \left(1 + \frac{1}{2\alpha q_0^2} \right)^{-\frac{3}{2}} \times \exp \left\{ -\frac{\alpha r_{jk}^2}{2\alpha q_0^2 + 1} - \frac{p_{jk}^2}{2p_0^2} \right\} \delta_{\tau_j \tau_k} \delta_{\sigma_j \sigma_k} \quad (2.23)$$

Table 2.1 Parameters of the hard equation of state implemented in the UrQMD model, with and without Pauli-potential.

parameter	without Pauli-potential	with Pauli-potential
$\alpha(fm^{-2})$	0.25	0.1152
$t_1(MeV fm^3)$	-7264.04	-84.5
$t_\gamma(MeV fm^6)$	87.65	188.2
γ	1.675	1.46
$V_0^{Yukawa}(MeV fm)$	-0.498	-85.1
γ_Y	1.4	1.0
$V_0^{Pauli}(MeV)$	-	98.95
$q_0(fm)$	-	2.16
$p_0(MeV/c)$	-	120

with

$$r_{jk} = \left| \vec{r}_j - \vec{r}_k \right| \quad (2.24)$$

and

$$p_{jk} = \left| \vec{p}_j - \vec{p}_k \right|. \quad (2.25)$$

In the UrQMD model only hard equation of state has been implemented and all parameters used are listed in Table 2.1. At present the generalization of two body forces to the relativistic region is not fully incorporated.

Note that these potential interactions are used in the model with relative momenta $\Delta p < 2 \text{ GeV}/c$. For the hadronic collisions with $\Delta p > 2 \text{ GeV}/c$ the potential interactions are omitted.

2.3 Cross sections

In each collisions, there are many kinds of particle being produced. The UrQMD model has capability to identify 55 different of baryon species (including nucleon, delta, hyperon and their resonances) with masses up to $2.25 \text{ GeV}/c^2$ and 32 different of meson species (including strange meson and its resonances). Their anti-particle and isospin-projected states can also be determined. Table 2.2 shows 6 types of baryons and their corresponding masses which can be found in the UrQMD. In Table 2.3, the meson and meson resonances, arranged by their spin and parity are given. The states listed can either be produced in string decays or resonance decays which will be described in the subsequent section.

The condition for hadron collision is

$$d < \sqrt{\frac{\sigma_{tot}}{\pi}} \quad (2.26)$$

where d represents the distance between two hadrons and σ_{tot} is total cross section of the two hadrons.

Within the UrQMD model the energy dependent cross sections of hadron-hadron interactions are importance and can be applied as basic input in the model. To weigh the difference decay channels the partial cross sections are used. In this section the important cross sections of baryon-antibaryon ($B\bar{B}$), baryon-baryon which used in this model, are displayed. For baryon-meson and meson-meson cross sections, one can see in (Bass et al., 1998; Bleicher et al., 1999). In case of unknown cross section, the additive quark model will be useful and briefly described in this section.

Table 2.2 Baryons and baryon-resonances included into the UrQMD model. Through baryon-antibaryon symmetry the respective antibaryon states are included as well.

Nucleon	Delta	Lambda	Sigma	Xi	Omega
N_{938}	Δ_{1232}	Λ_{1116}	Σ_{1192}	Ξ_{1315}	Ω_{1672}
N_{1440}	Δ_{1600}	Λ_{1405}	Σ_{1385}	Ξ_{1530}	
N_{1520}	Δ_{1620}	Λ_{1520}	Σ_{1660}	Ξ_{1690}	
N_{1535}	Δ_{1700}	Λ_{1600}	Σ_{1670}	Ξ_{1820}	
N_{1650}	Δ_{1900}	Λ_{1670}	Σ_{1750}	Ξ_{1950}	
N_{1675}	Δ_{1905}	Λ_{1690}	Σ_{1775}	Ξ_{2030}	
N_{1680}	Δ_{1910}	Λ_{1800}	Σ_{1915}		
N_{1700}	Δ_{1920}	Λ_{1810}	Σ_{1940}		
N_{1710}	Δ_{1930}	Λ_{1820}	Σ_{2030}		
N_{1720}	Δ_{1950}	Λ_{1830}			
N_{1900}		Λ_{1890}			
N_{1990}		Λ_{2100}			
N_{2080}		Λ_{2110}			
N_{2190}					
N_{2200}					
N_{2250}					

2.3.1 Baryon-antibaryon

One of the most importance of baryon-antibaryon interactions is the total cross-section which comes from the process of annihilation when energies $p_{lab} = 100\text{GeV}/c$. The earlier experiments on $\bar{p}p$ -annihilation revealed a number of differ-

Table 2.3 Mesons and meson-resonances, sorted with respect to spin and parity, included into the UrQMD model.

0^{-+}	1^{--}	0^{++}	1^{++}	1^{+-}	2^{++}	$(1^{--})^*$	$(1^{--})^{**}$
π	ρ	a_0	a_1	b_1	a_2	ρ_{1450}	ρ_{1700}
K	K^*	K_0^*	K_1^*	K_1	K_2^*	K_{1410}^*	K_{1680}^*
η	ω	f_0	f_1	h_1	f_2	ω_{1420}	ω_{1662}
η'	ϕ	f_0^*	f_1'	h_1'	f_2'	ϕ_{1680}	ϕ_{1900}

ences from the non-annihilation channels. It is not fully understood whether they come from the kinematic restrictions on the available phase space, or related to dynamical differences between the non-annihilation and annihilation mechanisms. In the experimental results (Zabrodin et al., 1995) the comparison between pp interactions and non-annihilation $\bar{p}p$ interactions at 32 GeV/c supported the conclusion of equivalence of pp interaction and non-annihilation $\bar{p}p$ interaction processes.

The UrQMD parameters are obtained from fitting the experimental data. For $\bar{p}p$ cross section, the data from Barnett's experiment (Barnett et al., 1996b) are used. Fig. 2.1 shows the UrQMD parameterizations comparing to the experiment (Barnett et al., 1996a). The total $\bar{p}p$ cross-sections correspond to a solid line. The annihilation cross-sections are exhibited by a dash line and elastic cross-sections are represented by a dot line.

In UrQMD model the $\bar{p}p$ total and elastic cross section derive from the CERN/HERA parameterizations and the annihilation cross section come from the Koch and Dover parameterizations.

The total and elastic $\bar{p}p$ cross-sections is given by

$$\sigma(p) = A + Bp^n + C \ln^2(p) + D \ln(p) \quad (2.27)$$

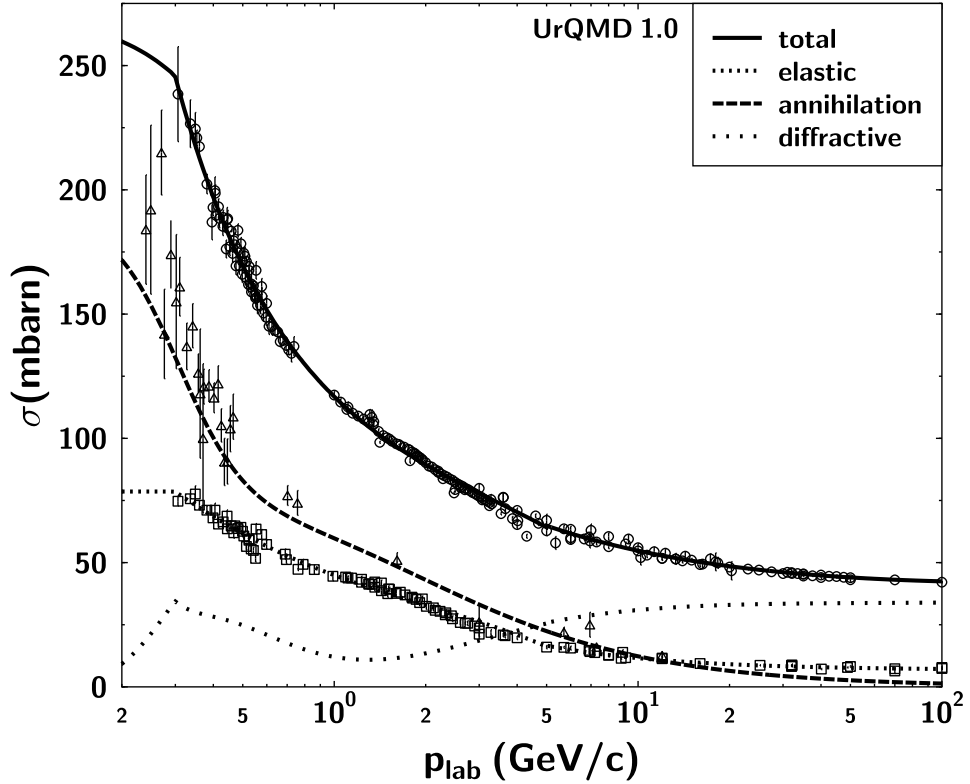


Figure 2.1 The $\bar{p}p$ cross-section as compared to the experimental data (Barnett et al., 1996a) on total (open circles), elastic (open squares), and annihilation (open triangles) cross-sections. The diffractive cross-section is assumed to be a difference between the total cross-section and the sum of the elastic and annihilation cross-section.

where p represents the laboratory-momentum in unit of GeV/c , σ represents the cross-section in unit of millibarn (mb). A, B, C and D are parameters which are some number show in Table 2.4.

For $p_{lab} < 5\text{GeV}/c$, UrQMD uses another parameterization to obtain the total and elastic cross section which are shown in Eq. (2.28) and (2.29), respec-

Table 2.4 Parameters for the CERN/HERA parameterization for the total and elastic antiproton -proton cross-sections. This parameterization is used in UrQMD for momenta $p_{lab} > 5\text{GeV}/c$.

σ	A	B	C	D	n
total	38.4	77.6	0.26	-1.2	-0.64
elastic	10.2	52.7	0.125	-1.28	-1.16

tively.

$$\sigma_{tot}(p) = \begin{cases} 75.0 + 43.1p^{-1} + 2.6p^{-2} - 3.9p & : 0.3 < p < 5 \\ 271.6 \exp(-1.1p^2) & : p < 0.3 \end{cases} \quad (2.28)$$

$$\sigma_{el}(p) = \begin{cases} 31.6 + 18.3p^{-1} - 1.1p^{-2} - 3.8p & : 0.3 < p < 5 \\ 78.6 & : p < 0.3 \end{cases} \quad (2.29)$$

The $\bar{p}p$ annihilation cross-section is given by Koch and Dover (Koch and Dover, 1989)

$$\sigma_{ann}^{\bar{p}p} = \sigma_0^N \frac{s_0}{s} \left[\frac{A^2 s_0}{(s - s_0)^2 + A^2 s_0} + B \right] \quad (2.30)$$

where $\sigma_0^N = 120 \text{ mb}$, $s_0 = 4m_N^2$, $A=50 \text{ MeV}$ and $B=0.6$.

In theory, the sum of annihilation and elastic cross-sections should be equal to the total cross-section. However, from experiment, the sum of annihilation and elastic cross-sections is smaller than the total cross section

$$\Delta\sigma = \sigma_{tot} - \sigma_{el} - \sigma_{ann} \quad (2.31)$$

The value of $\Delta\sigma$ is interpreted as the diffractive cross-section which describes the excitation at least one of the collision particles to a resonance or to a string via Pomeron exchange.

2.3.2 Baryon-baryon

In UrQMD the particles can be produced via the decay of a baryon resonance or meson resonance or via a string excitation and fragmentation. At the incident beam energies up to 8–10 GeV/nucleon the resonance decays is dominated for particle production. For the reaction $A + C \rightarrow D + E$, the total baryon-baryon cross-section is written as the form

$$\sigma_{tot}^{BB}(\sqrt{s}) \propto (2S_D + 1)(2S_E + 1) \frac{\langle p_{D,E} \rangle}{\langle p_{A,C} \rangle} \frac{1}{s} |\mathcal{M}(D, E)|^2, \quad (2.32)$$

where S_i is the spins of the particles and $|\mathcal{M}|^2$ is the matrix element. Here the matrix element $|\mathcal{M}|^2$ is a function of masses of outgoing particles (D, E). The $\langle p_{i,j} \rangle$ are the momenta of the pairs of particles in the two-particle rest frame defined as

$$\langle p_{i,j}(\sqrt{s}) \rangle = \frac{1}{2\sqrt{s}} \sqrt{(s - (m_i + m_j)^2)(s - (m_i - m_j)^2)}. \quad (2.33)$$

A detailed comparison on the baryon-baryon cross sections between the UrQMD and the experimental data (Barnett et al., 1996a) can be seen in (Bleicher et al., 1999).

2.3.3 The additive quark model

The additive quark model (AQM) (Close, 1979; Perkin, 1987) is used to calculate the unknown cross-sections. To calculate the unknown cross section one needs to know the cross-sections of the quark interactions, which can be evaluated from the quark masses. Next by assuming that a 40% reduced s -quark cross-section (compared to that of u - and d -quark), the unknown total cross-section of the high energy reaction can be calculated. Derived from the Regge theory (Goulianos, 1983), the elastic cross-section has the form:

$$\sigma_{\text{elastic}} = 0.039 \sigma_{\text{total}}^{\frac{3}{2}} [\text{mb}] \quad , \quad (2.34)$$

with

$$\sigma_{\text{total}} = 40 \left(\frac{2}{3}\right)^{m_1+m_2} \left(1 - 0.4 \frac{s_1}{3 - m_1}\right) \left(1 - 0.4 \frac{s_2}{3 - m_2}\right) [\text{mb}] \quad , \quad (2.35)$$

where $m_i = 1(0)$ for particle i being a meson (a baryon) and s_i is the number of strange quarks in particle i . For the meson-baryon and meson-meson interactions, their cross-sections are re-scaled by

$$\sigma_{X_1 X_2}(\sqrt{s}) = \frac{\sigma_{\pi N}(\sqrt{s})}{\sigma_{\pi N}^{\text{AQM}}} \sigma_{X_1 X_2}^{\text{AQM}} \quad . \quad (2.36)$$

Note that the non-strange baryon cross-sections are not treated via the additive quark model because they have an explicit energy dependence in line with experimental data.

2.4 Reaction channels

At high energy, the range of energy from the SIS ($\sqrt{s} \simeq 2$ GeV) up to the RHIC ($\sqrt{s} \simeq 200$ GeV), a huge number of different particle types can be produced and can interact further with each other. In this range of energy the potentials, which introduced in section 2.2, can be omitted. At energy lower than $\sqrt{s} = 5$ GeV for baryon-baryon and 3 GeV for meson-baryon and meson-meson, the particles mainly produced via the production and decay of resonances. However, above 3.5 GeV the contribution of cross sections become less important because the string and multiple decay channels open and allow for multiple resonance production.

In this section, the ways of particle production at high energy via baryon-baryon collisions are explained as the subsection resonances. Moreover the particle production at high energy regime and from baryon-antibaryon production can be described in the string model.

2.4.1 Resonances

To produce the baryon resonances, one has to consider the two different ways:

- i) hard production: $N+N \rightarrow \Delta N, \Delta\Delta, N^*N$, etc.
- ii) soft production: $\pi^-+p \rightarrow \Delta^0, K^-+p \rightarrow \Lambda^* \dots$.

Here the cross sections for the non-strange processes, $NN \rightarrow N\Delta_{1232}$, $NN \rightarrow NN^*$, $NN \rightarrow N\Delta^*$, $NN \rightarrow \Delta_{1232}\Delta_{1232}$, $NN \rightarrow \Delta_{1232}N^*$ and $NN \rightarrow \Delta_{1232}\Delta^*$, are included in order to produce resonance particles. After the numbers of the excited resonance has been assigned, its mass and properties must be determined. Table 2.5 shows the masses in unit of GeV/c^2 , widths in unit of MeV and branching ratios of non-strange baryon-resonances which used in the UrQMD model. Also the properties of single- and double-strange baryon resonances are listed respectively in Table 2.6 and 2.7. For the meson-resonances one has to see in (Bass et al., 1998). Note that the strange particles can be produced by the soft production, for example, $K^- + p \rightarrow \Lambda^* + X$, etc.

2.4.2 Strings

To describe the baryon-antibaryon annihilation and the particles production at high energy, the string model (Andersson et al., 1982) is applied and included in the UrQMD model. The string model is originated from the idea that at sufficiently large distances the color field between two quarks or anti-quarks can be transformed into the color string. In baryon-baryon interaction strings between quark q_i and diquark qq_i from the same baryon are produced. Also for meson-meson interaction the string between quark q_i and antiquark \bar{q}_i are produced from the same meson. As the same way as baryon, the string between antiquark \bar{q}_i

Table 2.5 Masses (GeV/c^2), widths (MeV) and branching ratios of non-strange baryon-resonances in UrQMD. All parameters are within the range given by the Review of Particle Properties (Barnett et al., 1996a).

resonance	mass	width	N_γ	N_π	N_η	N_ω	N_ρ	$N_{\pi\pi}$	$\Delta_{1232\pi}$	$N_{1440\pi}^*$	ΛK
N_{1440}^*	1.440	200		0.70				0.05	0.25		
N_{1520}^*	1.520	125		0.60				0.15	0.25		
N_{1535}^*	1.535	150	0.001	0.55	0.35			0.05		0.05	
N_{1650}^*	1.650	150		0.65	0.05			0.05	0.10	0.05	0.10
N_{1675}^*	1.675	140		0.45					0.55		
N_{1680}^*	1.680	120		0.65				0.20	0.15		
N_{1700}^*	1.700	100		0.10	0.05		0.05	0.45	0.35		
N_{1710}^*	1.710	110		0.15	0.20		0.05	0.20	0.20	0.10	0.10
N_{1720}^*	1.720	150		0.15			0.25	0.45	0.10		0.05
N_{1900}^*	1.870	500		0.35		0.55	0.05		0.05		
N_{1990}^*	1.990	550		0.05			0.15	0.25	0.30	0.15	0.10
N_{2080}^*	2.040	250		0.60	0.05		0.25	0.05	0.05		
N_{2190}^*	2.190	550		0.35			0.30	0.15	0.15	0.05	
N_{2220}^*	2.220	550		0.35			0.25	0.20	0.20		
N_{2250}^*	2.250	470		0.30			0.25	0.20	0.20	0.05	
Δ_{1232}	1.232	115.	0.01	1.00							
Δ_{1600}^*	1.700	200		0.15					0.55	0.30	
Δ_{1620}^*	1.675	180		0.25					0.60	0.15	
Δ_{1700}^*	1.750	300		0.20			0.10		0.55	0.15	
Δ_{1900}^*	1.850	240		0.30			0.15		0.30	0.25	
Δ_{1905}^*	1.880	280		0.20			0.60		0.10	0.10	
Δ_{1910}^*	1.900	250		0.35			0.40		0.15	0.10	
Δ_{1920}^*	1.920	150		0.15			0.30		0.30	0.25	
Δ_{1930}^*	1.930	250		0.20			0.25		0.25	0.30	
Δ_{1950}^*	1.950	250	0.01	0.45			0.15		0.20	0.20	

and anti-diquark $\bar{q}\bar{q}_i$ from the antibaryon can be produced. Here the linear string potential between the quark and diquark, which located at respectively z_1 and z_2 , has the form

$$V_1 = \kappa |z_1 - z_2| \quad , \quad (2.37)$$

Table 2.6 Masses (GeV/c^2), widths (MeV) and branching ratios of single-strange baryon-resonances in UrQMD. All parameters are within the range given by the Review of Particle Properties (Barnett et al., 1996a).

resonance	mass	width	$N\bar{K}$	$N\bar{K}_{892}^*$	$\Sigma\pi$	$\Sigma^*\pi$	$\Lambda\eta$	$\Lambda\omega$	$\Lambda\pi$	$\Sigma\eta$	$\Lambda^*\pi$	$\Delta\bar{K}$
Λ_{1405}^*	1.407	50			1.00							
Λ_{1520}^*	1.520	16	0.45		0.43	0.11						
Λ_{1600}^*	1.600	150	0.35		0.65							
Λ_{1670}^*	1.670	35	0.20		0.50		0.30					
Λ_{1690}^*	1.690	60	0.25		0.45	0.30						
Λ_{1800}^*	1.800	300	0.40	0.20	0.20	0.20						
Λ_{1810}^*	1.810	150	0.35	0.45	0.15	0.05						
Λ_{1820}^*	1.820	80	0.73		0.16	0.11						
Λ_{1830}^*	1.830	95	0.10		0.70	0.20						
Λ_{1890}^*	1.890	100	0.37	0.21	0.11	0.31						
Λ_{2100}^*	2.100	200	0.35	0.20	0.05	0.30	0.02	0.08				
Λ_{2110}^*	2.110	200	0.25	0.45	0.30							
Σ_{1385}^*	1.384	36			0.12				0.88			
Σ_{1660}^*	1.660	100	0.30		0.35				0.35			
Σ_{1670}^*	1.670	60	0.15		0.70				0.15			
Σ_{1750}^*	1.750	90	0.40		0.05					0.55		
Σ_{1775}^*	1.775	120	0.40		0.04	0.10			0.23		0.23	
Σ_{1915}^*	1.915	120	0.15		0.40	0.05			0.40			
Σ_{1940}^*	1.940	220	0.10	0.15	0.15	0.15			0.15		0.15	0.15
Σ_{2030}^*	2.030	180	0.20	0.04	0.10	0.10			0.20		0.18	0.18

where κ is the string tension. This form of potential is supported by the lattice QCD calculation (Born et al., 1994).

From the string potential, the hamiltonian can be written in the form

$$H = |p_1| + |p_2| + \kappa|z_1 - z_2| \quad , \quad (2.38)$$

which leads to the following equations of motion for the massless endpoints of the

Table 2.7 Masses (GeV/c²), widths (MeV) and branching ratios of double-strange baryon-resonances in UrQMD. All parameters are within the range given by the Review of Particle Properties (Barnett et al., 1996a).

resonance	mass	width	$\Xi\pi$	$\Xi\gamma$	$\Lambda\bar{K}$	$\Sigma\bar{K}$
Ξ_{1530}^*	1.532	9	0.98	0.02		
Ξ_{1690}^*	1.700	50	0.10		0.70	0.20
Ξ_{1820}^*	1.823	24	0.15		0.70	0.15
Ξ_{1950}^*	1.950	60	0.25		0.50	0.25
Ξ_{2030}^*	2.025	20	0.10		0.20	0.70

string:

$$\frac{dp_i}{dt} = -\frac{\partial H}{\partial z_i} = -\text{sign}(z_i - z'_i) \kappa \quad , \quad (2.39)$$

$$\frac{dz_i}{dt} = +\frac{\partial H}{\partial p_i} = \text{sign}(p_i) \quad , \quad (2.40)$$

where the sign of $(z_i - z'_i)$ is related to a change in momentum while the direction of propagation is defined by the sign of the momentum p_i of the quark.

With large momentum transfer, the excitation of the string may exceed some critical limit. Then the string is broken into pieces by producing $q\bar{q}$ -pairs from the vacuum. Each of the produced $q\bar{q}$ -pairs will have small relative momenta in their rest frame. Owing to the fact that the color string is uniformly stretched, the hadrons produced as a result of the string fragmentation will be uniformly distributed within the kinematically allowed interval between $y_{min} = 0$ and $y_{max} = \ln(s/m_T^2)$.

For the creation of a quark-antiquark pair with mass m in a color field with



Figure 2.2 Particle production in a string.

Table 2.8 Probabilities for the different meson-multiplets in the UrQMD model.

multiplet J^{PC}	0^{-+}	1^{--}	0^{++}	1^{++}	2^{++}	1^{+-}	1^{--*}	1^{--**}
probability	0.102	0.190	0.056	0.124	0.197	0.127	0.110	0.095

a string tension κ , its probability $|M|^2$ can be written as

$$|M|^2 = \text{constant} \times \exp\left(-\frac{\pi m^2}{\kappa}\right), \quad (2.41)$$

where a typical value for κ is 1 GeV/fm (Andersson et al., 1982; Andersson et al., 1983). This probability is introduced by Schwinger's QED-based result for particle-antiparticle creation in a strong electric field (Schwinger, 1951).

An example view of the particles production in a string is shown in Fig. 2.2. The linked quark and diquark (non-strange) with string tension κ is depicted on the left hand side. After that the two pairs of $s\bar{s}$ and $u\bar{u}$ are created from the vacuum. Here the diquark can be combined with a newly s quark to form a hyperon, the newly \bar{s} and u quarks form to be a kaon and a newly \bar{u} with a quark at the endpoint of string to be a pion.

In the UrQMD, for baryon, the states which type of hadron is produced, not be determined from the quark configuration then the baryon octet and baryon decuplet are selected as equal probability. For higher excited multiplets the probabilities are tuned to the measured multiplicities of proton-proton reactions. In the case of meson the multiplet is determined before the identification of the particle types. Its probability depend on the spin of the multiplet and its average mass

$$P_{\text{multiplet}} \propto \frac{2S + 1}{\langle m \rangle_{\text{multiplet}}}. \quad (2.42)$$

The respective values for the meson multiplets which included in the UrQMD model, are listed in Table 2.8.

The detail of model that described in this chapter will be used to calculate the reaction of antiproton-nucleus as can be seen in the next chapter.

CHAPTER III

STRANGE PARTICLE AND NON-STRANGE PARTICLE PRODUCTION

Quantum Chromodynamics (QCD) is the well accepted theory to describe the physics of strong interaction. However, for low and medium energy reactions where the distance scale is on the order of $1/\Lambda_{\text{QCD}}$, interactions among quarks and gluons become so strong ($\alpha_s \sim 0.1$) that perturbative methods can not be applied anymore and one has to deal with QCD in non-perturbative approaches. Aiming at the exploration of the non-perturbative features of QCD antiproton annihilations on nuclear targets will be performed by the PANDA (antiProton ANihilation at DArmstadt) experiment at the currently-built Facility for Antiproton and Ion Research (FAIR) (GSI, 2001).

As reviewed in chapter I, the investigation of double Λ hypernuclei is one of the major physics topics of PANDA together with the exploration of exotic charm and gluon states. The production of double Λ hypernuclei is based on the capture reaction $\Xi^- + p \rightarrow \Lambda\Lambda$. Where the initial hyperon pair $\Xi\bar{\Xi}$ can be produced in a primary antiproton+nucleus interaction (Pochodzalla, 2005). In this chapter we set the stage for further studies of hypernuclei by exploring the production rates of strange and non-strange particles in antiproton-nucleus collisions. This chapter is arranged as follows: in section 3.1, we employ the UrQMD model to calculate the productions of strange particles (Σ and Λ) and compare the results to experimental data. Section 3.2 shows the results on the creation of non-strange particles. The UrQMD predictions for Ξ production are given in section 3.3.

3.1 UrQMD results on strange particle production

In this section we use the Ultra-relativistic Quantum Molecular Dynamics (UrQMD) model (Bass et al., 1998; Bleicher et al., 1999; Petersen et al., 2008), as described in chapter II, to calculate the yields, transverse momentum and rapidity spectra of strange particles in \bar{p} +nucleus collisions and compare the theoretical results with experimental data. The UrQMD approach is based on the covariant propagation of all incoming and secondary hadrons. It includes the annihilation of anti-baryons on baryons as well the subsequent interaction of strange particles with the nuclear matter.

The experimental study of $\bar{p} + {}^7\text{Li}$, ${}^{12}\text{C}$, ${}^{32}\text{S}$, ${}^{64}\text{Cu}$ collisions has been performed at the Serpukhov proton synchrotron which is located in Russia. Within this experiment, an unseparated beam of negatively charged particles with momenta of 40 GeV/c is used as an incident beam composed of a mixture of π^- , K^- and \bar{p} in the ratio of 100 : 1.8 : 0.3 (Boos et al., 1984; Grigalashvili et al., 1999). The nuclear targets were placed in the sensitive volume of relativistic ionization streamer chamber (RISC) along the beam line as depicted in Fig. 3.1. In the experiment the average multiplicities of neutral hyperons, $\Lambda(\Sigma^0)$ and $\bar{\Lambda}(\bar{\Sigma}^0)$ were investigated in the following reactions:

$$\bar{p} + A \rightarrow \Lambda(\Sigma^0) + X, \quad (3.1)$$

$$\bar{p} + A \rightarrow \bar{\Lambda}(\bar{\Sigma}^0) + X, \quad (3.2)$$

where A stand for ${}^7\text{Li}$, ${}^{12}\text{C}$, ${}^{32}\text{S}$ and ${}^{64}\text{Cu}$. Shown in Table 3.1 are our results as derived from the UrQMD model, compared with the experimental data (Grigalashvili et al., 1999). We find that the UrQMD results, for $\Lambda(\Sigma^0)$ and $\bar{\Lambda}(\bar{\Sigma}^0)$ production in the reactions $\bar{p} + \text{Li}$, C and S , slightly underestimate the experimental results (but are within the error bars) while for the $\bar{p} + \text{Cu}$ reaction the UrQMD results

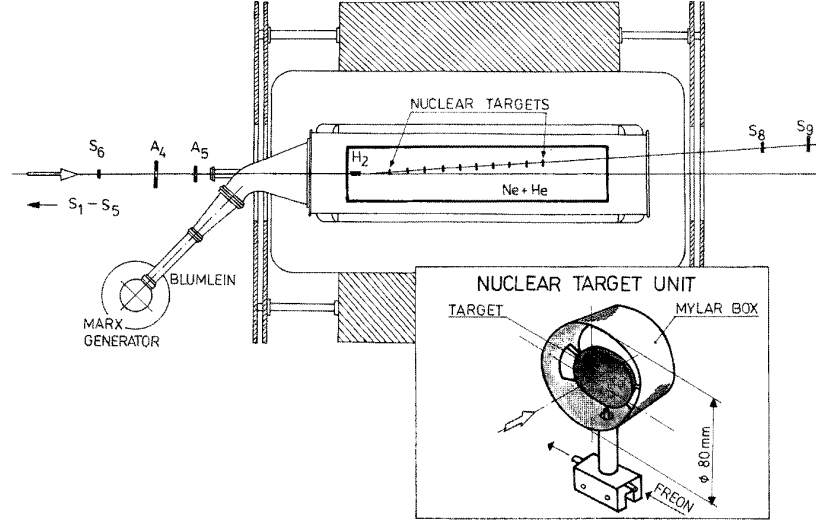


Figure 3.1 Layout of experiment at Serpukhov proton synchrotron (Boos et al., 1984).

slightly exceed the experimental data within the given errors. With increasing the mass of nuclear targets, the yields of $\Lambda(\Sigma^0)$ also increase while the multiplicities of anti-hyperons, $\bar{\Lambda}(\bar{\Sigma}^0)$, remain approximately constant. Considering the experimental errors, however, the UrQMD predictions for the averaged multiplicities of both $\Lambda(\Sigma^0)$ and $\bar{\Lambda}(\bar{\Sigma}^0)$ are in line with the experimental data.

Table 3.1 Comparison between experimental data (Grigalashvili et al., 1999) and UrQMD results for the average multiplicities of $\Lambda(\Sigma^0)$ and $\bar{\Lambda}(\bar{\Sigma}^0)$.

Target	$\langle n_{\Lambda(\Sigma^0)} \rangle$		$\langle n_{\bar{\Lambda}(\bar{\Sigma}^0)} \rangle$	
	Exp.	UrQMD	Exp.	UrQMD
Li	0.07 ± 0.01	0.06	0.06 ± 0.01	0.05
C	0.08 ± 0.02	0.07	0.06 ± 0.02	0.06
S	0.13 ± 0.01	0.11	0.07 ± 0.01	0.06
Cu	0.15 ± 0.02	0.17	0.05 ± 0.02	0.06

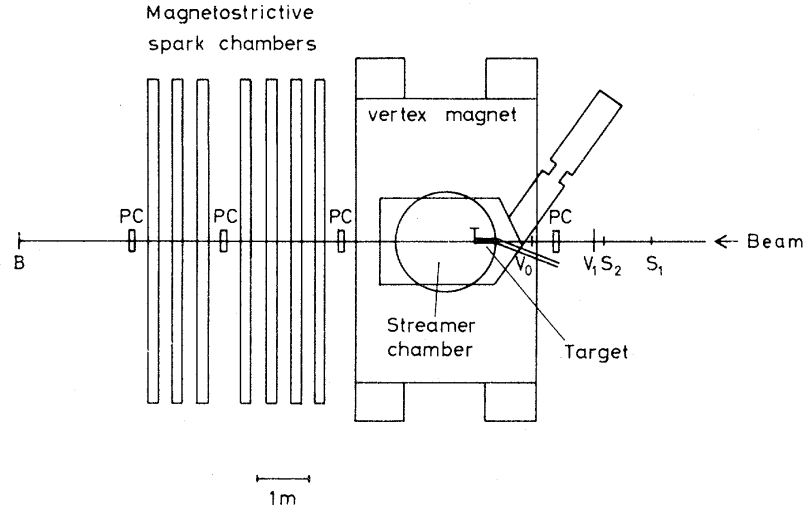


Figure 3.2 Layout of NA5 experiment at CERN SPS (De Marzo et al., 1982).

Next, we focus on the production of Λ and K^0 in the reaction $\bar{p} + {}^{131}\text{Xe}$ at a \bar{p} beam energy of 200 GeV (Derado et al., 1991). These experiments have been performed by the NA5 collaboration at the European Organization for Nuclear Research (CERN) Super Proton Synchrotron (SPS) using a streamer chamber inside a 1.5 Tesla superconductor vertex magnet (De Marzo et al., 1982). The layout of experiment is shown schematically in Fig. 3.2. The dimension of the streamer chamber were $2 \times 1.4 \times 0.72 \text{ m}^3$. Inside the streamer chamber, target of Xe was installed in form of gas tube, 55 centimeter long and 3 centimeter in diameter. Cherenkov counters were used to separate the H_2 beam at 200 GeV into beams of proton and antiproton at 200 GeV and used as projectile.

Table 3.2 shows the comparison between the NA5 experimental data (Derado et al., 1991) and UrQMD calculations on the average abundances of Λ , K^0 , negative hadrons (h^-), and the ratios $\langle n_\Lambda \rangle / \langle n_{h^-} \rangle$ and $\langle n_{K^0} \rangle / \langle n_{h^-} \rangle$. Again, one observes that the UrQMD calculations provide a satisfactory description of the experimental results.

To obtain more insights, we compare UrQMD results with experimental

Table 3.2 Comparison between experimental data by the NA5 collaboration (Derado et al., 1991) and UrQMD results on average multiplicities of Λ , K^0 , negative hadrons (h^-) and ratios.

	$\langle n_\Lambda \rangle$	$\langle n_{K^0} \rangle$	$\langle n_{h^-} \rangle$	$\langle n_\Lambda \rangle / \langle n_{h^-} \rangle$	$\langle n_{K^0} \rangle / \langle n_{h^-} \rangle$
Exp.	0.261 ± 0.04	0.610 ± 0.096	8.54 ± 0.15	0.031 ± 0.005	0.071 ± 0.011
UrQMD	0.228	0.695	8.54	0.027	0.081

data for the transverse momentum distributions and normalized laboratory rapidity distributions ($\frac{1}{N} \frac{1}{p_t} \frac{dN}{dp_t}$ and $\frac{1}{N} \frac{dN}{dy}$) with N being the number of event and p_t being the transverse momentum and y denoting the rapidity (Derado et al., 1991), also can be seen in appendix C for more detail. The transverse momentum distributions of Λ and K^0 are illustrated in Fig. 3.3 (upper panels). It appears that the UrQMD calculations slightly underestimate the Λ production at higher momenta (p_t larger than 1.2 GeV/c) while the K^0 production at low momenta (p_t less than 0.5 GeV/c) are slightly lower in UrQMD as compared to the data. Considering the large experimental errors, however, one can still conclude that the UrQMD calculation are in line with the experimental data.

The lower-right panel of Fig. 3.3 depicts the comparison between experimental data and UrQMD results on the normalized laboratory rapidity distributions. It is found that the UrQMD result agree with the experimental data for the K^0 production. The positively-skewed, bell-shaped K^0 rapidity distribution reveals that the K^0 are dominantly produced in the target fragmentation region.

The target fragmentation region is referred to the production of particles mainly from the target particle. In the other hand, the projectile fragmentation region is used to describe the production of particles mainly from the beam par-

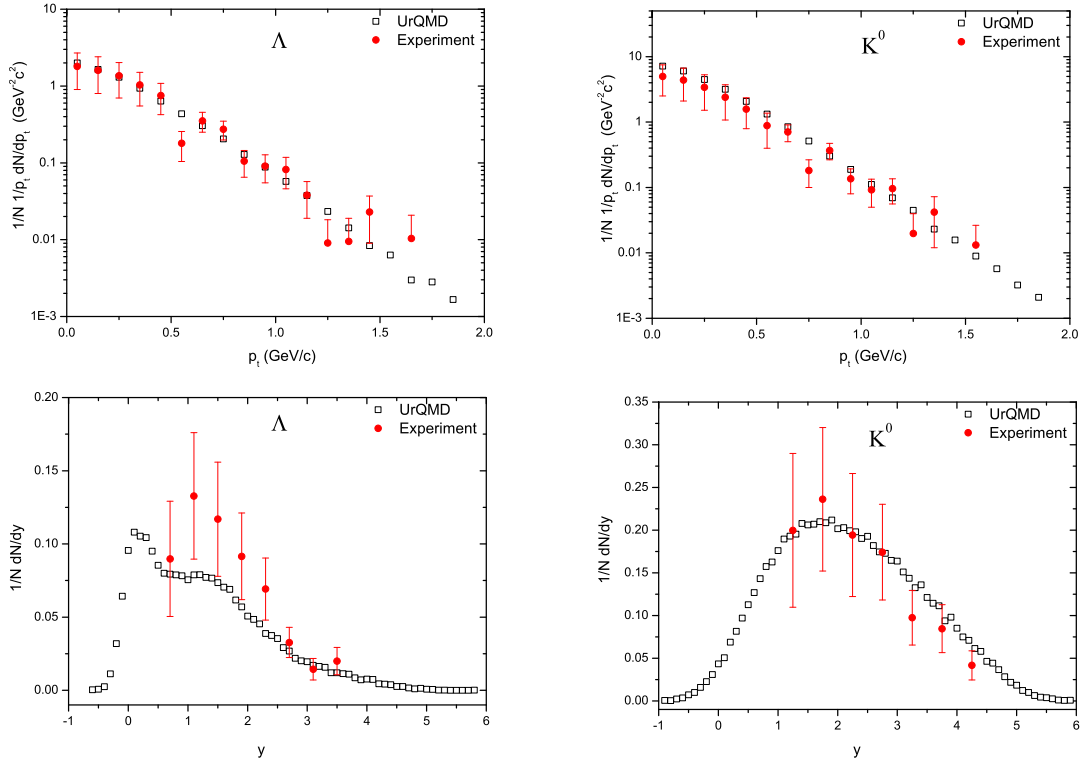


Figure 3.3 UrQMD results compared with experimental data (Derado et al., 1991) for transverse momentum distributions (upper panels) and normalized laboratory rapidity distributions (lower panels). Here the Λ (left panels) and the K^0 (right panels) are produced in $\bar{p} + \text{Xe}$ reaction at 200 GeV.

ticle in the forward direction. To describe the direction of produced particle, the rapidity,

$$y = \frac{1}{2} \ln \left(\frac{E + p_z}{E - p_z} \right), \quad (3.3)$$

is used. For our case, the Xe target in laboratory frame gives the initial rapidity $y_{Xe} = 0$ while the initial rapidity of \bar{p} is calculated from the relation,

$$y_{\bar{p}} = \sinh^{-1}(p_{\text{lab}}/m_{\bar{p}}), \quad (3.4)$$

to be 6. The central rapidity region is around 3. Therefore, that the K^0 are mainly produced with rapidity around 1.5 indicates that the K^0 are mainly produced in the target fragmentation region. The Λ rapidity distribution in Fig. 3.3 (lower-left

panel) shows that the UrQMD calculations underestimate the yield of Λ in the central rapidity region and the target fragmentation region. However, one should note that also here the experimental data suffers from substantial errors. In this case the central rapidity is calculated to be 3 from the initial rapidity 0 of Xe target and the initial rapidity 6 of \bar{p} . The UrQMD predicted peak at $y \sim 0$ indicates the ejection of Λ happens mainly in the target fragmentation region.

3.2 UrQMD results on non-strange particle production

Experimentally, reactions of $\bar{p} + {}^{24}\text{Mg}$, ${}^{108}\text{Ag}$ and ${}^{197}\text{Au}$ at \bar{p} momenta of 100 GeV/c have been performed at Fermilab in the experiment E597 with the Fermilab 30-inch bubble chamber (BC) and Downstream Particle Identifier (DPI), as shown in Fig. 3.4, to study the production of inclusive charged pion spectra (Whitmore et al., 1994). To compare to this data, we employ the UrQMD model and explore the production of π^\pm in the reactions:

$$\bar{p} + Mg \rightarrow \pi^\pm + X, \quad (3.5)$$

$$\bar{p} + Ag \rightarrow \pi^\pm + X, \quad (3.6)$$

$$\bar{p} + Au \rightarrow \pi^\pm + X. \quad (3.7)$$

The comparison between the experimental data and the UrQMD predictions on p_t^2 distributions is shown in Fig. 3.5. The left and right panel depict for the π^- and π^+ productions respectively. Fig. 3.5(a) and 3.5(b) indicate for the $\bar{p} + \text{Mg}$ reactions, Fig. 3.5(c) and 3.5(d) represent for $\bar{p} + \text{Ag}$ reactions and the reactions $\bar{p} + \text{Au}$ are presented by the Fig. 3.5(e) and 3.5(f). As shown in these figures the results for Mg, Ag and Au targets are quite similar. The UrQMD calculations agree well with the experimental data on the transverse momentum spectra of π^- . In case of π^+ , at low p_t^2 , the UrQMD results are in line with the

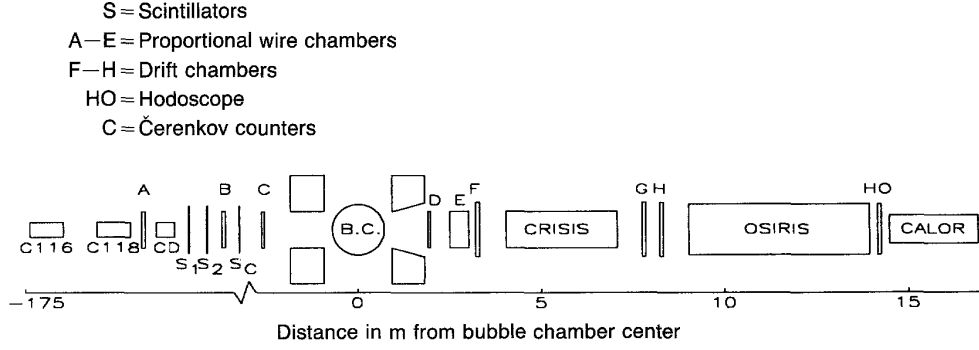


Figure 3.4 Layout of Fermilab 30-inch bubble chamber spectrometer and downstream particle identifier (Whitmore et al., 1994).

experimental data, while a slight deviation from the data is observed towards high p_t^2 . However, one may note that π are mainly produced at low momenta.

3.3 Model predictions for $\Xi\bar{\Xi}$ production

As seen in the section 3.1 and 3.2, UrQMD reproduces the experimental data of strange and non-strange particles reasonably well. Thus, one can conclude that the UrQMD model is a suitable tool to predict strange particle spectra and abundancies in antiproton-nucleus collisions. In this section we employ the UrQMD model to provide information of productions of the multi-strange hyperons $\Xi\bar{\Xi}$ which are the important ingredients for double Λ hypernuclei formation. Fig. 3.6 depicts the multiplicities of Ξ^- and $\bar{\Xi}^+$ as calculated in the UrQMD model for the reactions $\bar{p} + {}^{24}\text{Mg}$, ${}^{64}\text{Cu}$ and ${}^{197}\text{Au}$ at center-of-mass energies from 3 to 4 GeV. It is found that the multiplicities of Ξ^- are very similar for the different targets but significantly increase with increasing center-of-mass energy. The multiplicities of $\bar{\Xi}^+$ are considerably different for different reactions. The multiplicity of $\bar{\Xi}^+$ produced with the Mg target is clearly higher than the $\bar{\Xi}^+$ from Cu target, and the multiplicity of $\bar{\Xi}^+$ from the Au target is almost zero for the whole inspected

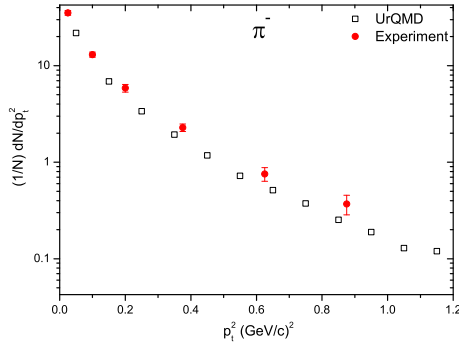
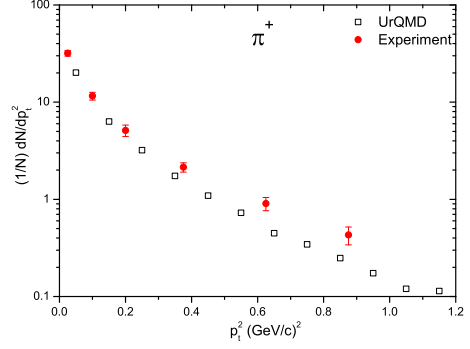
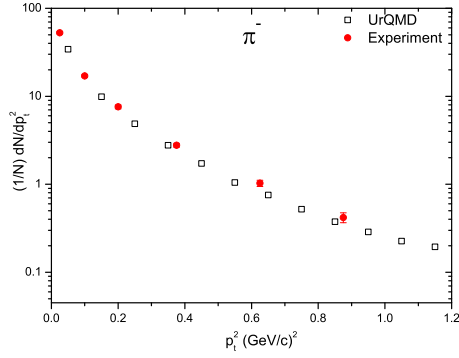
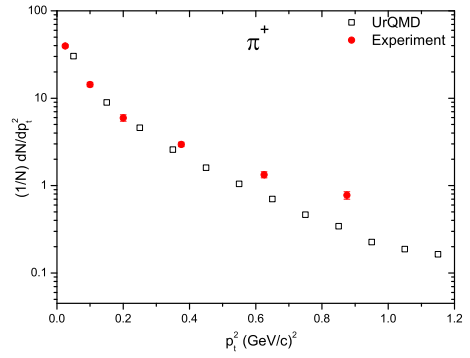
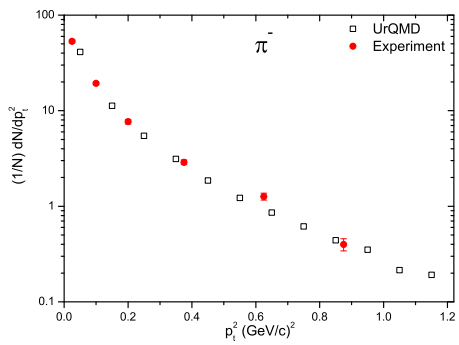
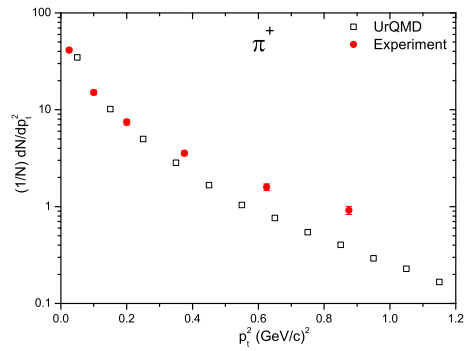
(a) $\bar{p} + Mg \rightarrow \pi^- + X$ (b) $\bar{p} + Mg \rightarrow \pi^+ + X$ (c) $\bar{p} + Ag \rightarrow \pi^- + X$ (d) $\bar{p} + Ag \rightarrow \pi^+ + X$ (e) $\bar{p} + Au \rightarrow \pi^- + X$ (f) $\bar{p} + Au \rightarrow \pi^+ + X$

Figure 3.5 UrQMD results compared with experimental data (Whitmore et al., 1994) for p_t^2 distributions of π^- (left panels) and π^+ (right panels) produced in $\bar{p} + Mg$, Ag and Au at a \bar{p} momentum of $100 \text{ GeV}/c$.

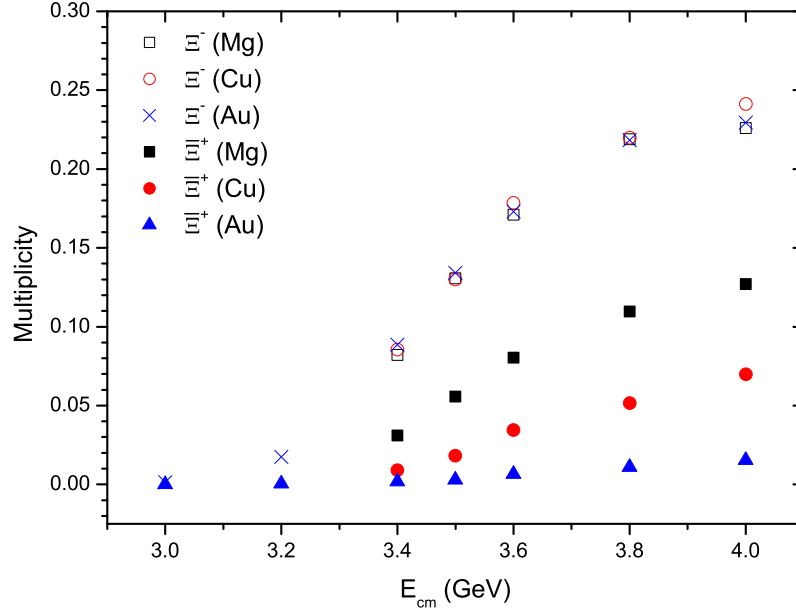


Figure 3.6 Multiplicities of Ξ^- and Ξ^+ from the reactions of $\bar{p} + \text{Mg}$, Cu and Au collisions.

energy region. This observation can be well understood, because a bigger-sized nucleus provides a higher chance for a Ξ^+ to be absorbed by subsequent collisions with the nucleons. The predicted multiplicities provide useful information for the trigger condition for double Λ hypernuclei production.

In next chapter, we will apply this method to investigate the double Λ hypernuclei production. The deeply calculation on the trigger conditions, deceleration mechanism and hyperon induced reactions will be described.

CHAPTER IV

HYPERNUCLEUS PRODUCTION

To perform the quantitative analysis we apply the Ultra-relativistic Quantum Molecular Dynamics (UrQMD) model. A comparison of the model to data in anti-proton induced reactions can be found in chapter III and also in (Limphirat et al., 2009; Galoyan and Polanski, 2003), a study on hyperon production at low energies has been performed in (Zeeb et al., 2004).

Due to the lack of data on Ξ and Ω production in $\bar{p} + p$ reactions it is difficult to establish a solid baseline for the multiplicity of multi-strange baryons in the relevant energy regime. In the following we will trigger on the production of a Ξ in the initial $\bar{p} + p$ reaction and leave the absolute normalization aside.

In this chapter, we begin by investigating the trigger condition for Ξ^- production. Then in section 4.2 we explain the deceleration mechanism of Ξ^- inside the primary nucleus. The produced Ξ^- interacts with the secondary nucleus will be described in section 4.3.

4.1 Experimental trigger conditions

Let us start with an investigation of the experimental trigger condition for the desired event. Here events are signalled by the measurement of the Ξ^+ or a K^+K^+ pair. In this work, the productions of Ξ^+ and K^+K^+ pair are investigated in $\bar{p}+\text{Au}$ collisions, based on the reaction

$$\bar{p} + \text{Au} \rightarrow \Xi + \bar{\Xi} + \text{X}. \quad (4.1)$$

To reduce the background from associated particles, the center-of-mass energies are taken from 3 to 4 GeV, which are closed to the threshold energy of $\Xi\bar{\Xi}$ production. Shown in Fig. 4.1 are the multiplicities of Ξ s, $\bar{\Xi}$ s and K^+K^+ pair productions in \bar{p} +Au collisions at the energy region from 3 to 4 GeV. The solid square, solid circle, open triangle and open diamond symbols indicate respectively the multiplicities of Ξ^- , Ξ^0 , $\bar{\Xi}^+$ and $\bar{\Xi}^0$ while the open squares denote the multiplicity of K^+K^+ pair. It is found that the multiplicities of Ξ and K^+K^+ pair are significantly increased with increasing energy while the multiplicities of $\bar{\Xi}$ s are very close to zero in the whole energy region. One may conclude that the produced $\bar{\Xi}$ have been absorbed by consequent collisions with nucleons in the Au target, and the di-Kaon trigger has observant advantage over the $\bar{\Xi}$ trigger.

To effectively detect the K^+K^+ pair productions by the anti-hyperon absorption in the primary nucleus target:

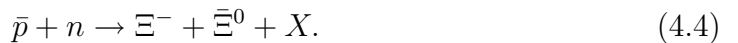


one needs information of the momentum distribution of K^+ from the produced K^+K^+ pairs. Fig. 4.2 shows the lab momentum distribution of K^+ from the produced K^+K^+ pairs in the \bar{p} +Au reactions at $\sqrt{s} = 4$ GeV. It is found that the production of K^+ from K^+K^+ pairs peaks at lab momentum around 0.3 GeV/c.

Next we look at the \sqrt{s} distribution of the antibaryon-baryon processes that lead to the production of a Ξ^- baryon (see Fig. 4.3). Note that the Ξ^- can be produced from the reactions



and



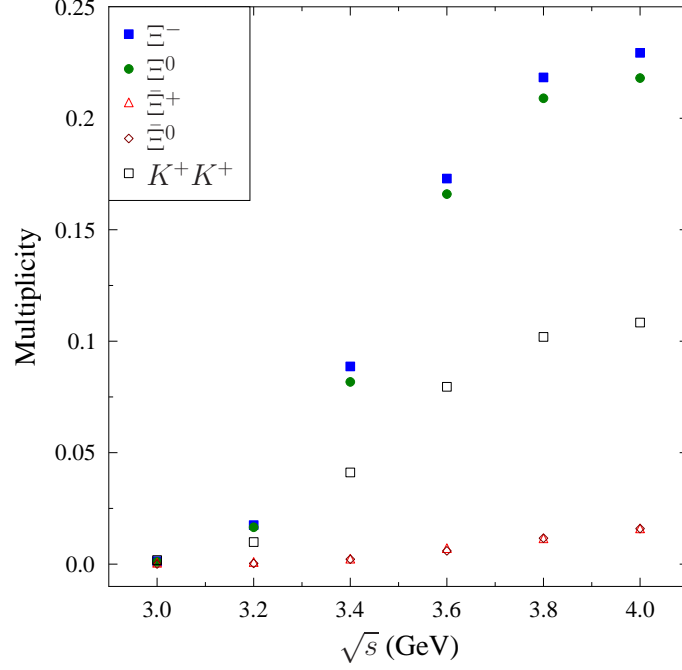


Figure 4.1 Multiplicity comparison between the Ξ , $\bar{\Xi}$ and the K^+K^+ pair in \bar{p} +Au reactions at center of mass energies from 3 to 4 GeV. The solid square, solid circle, open triangle and open diamond symbols indicate respectively the multiplicities of Ξ^- , Ξ^0 , $\bar{\Xi}^+$ and $\bar{\Xi}^0$ while the open squares denote the multiplicity of K^+K^+ pair.

The plots in Fig. 4.3 are for the \bar{p} +Au reactions at $\sqrt{s} = 4$ GeV, where the square and circle symbols denote the \sqrt{s} distributions of the $\bar{p} + p \rightarrow \Xi^- + \bar{\Xi}^+ + X$ channel and the $\bar{p} + n \rightarrow \Xi^- + \bar{\Xi}^0 + X$ channel, respectively. It is found in Fig. 4.3 that Ξ^- are highly produced at a quite large $\sqrt{s}_{\bar{B}B}$ range (from 3.5 to 4.3 GeV) for both the channels and that around $\sqrt{s}_{\bar{B}B} = 4$ GeV the Ξ^- production in the process $\bar{p} + n \rightarrow \Xi^- + \bar{\Xi}^+ + X$ is almost double the one in the $\bar{p} + p \rightarrow \Xi^- + \bar{\Xi}^+ + X$ channel. Here one sees that the Fermi motion leads to a smearing of the energy, making it hard to predict the exact kinematics of the produced Ξ^- .

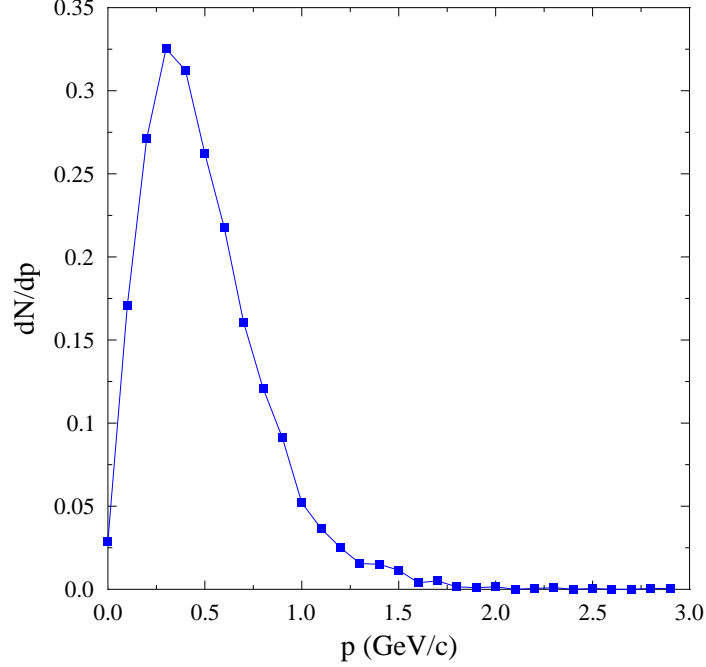


Figure 4.2 Momentum distribution of K^+ (from K^+K^+ pair) in \bar{p} +Au reactions at $\sqrt{s} = 4$ GeV.

4.2 Deceleration mechanism

If the Ξ^- has been produced it undergoes multiple scatterings in the nucleus. On average, each Ξ^- scatters three times before leaving the nucleus. This distribution of the number of scatterings is depicted in Fig. 4.4. Here, the Ξ^- are produced in \bar{p} +Au reactions at $\sqrt{s} = 4$ GeV.

The subsequent re-scattering of the Ξ^- leads to a substantial deceleration of Ξ^- in comparison to the $\bar{p} + p$ reactions at the same energy. The comparison of momentum spectra of the Ξ^- between $\bar{p} + p$ and \bar{p} +Au reactions are shown in Fig. 4.5. Due to the deceleration of Ξ^- by re-scattering inside the primary nucleus, the Ξ^- are mainly created with momentum around 0.2 GeV/c from the

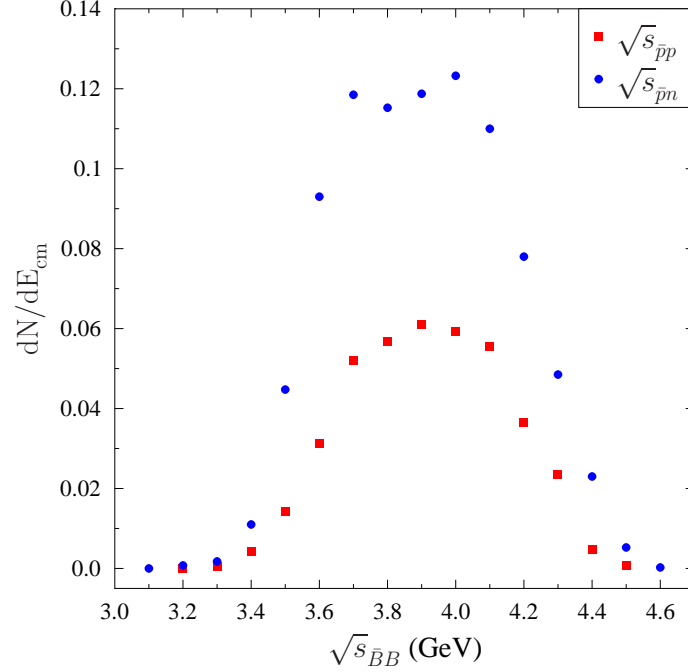


Figure 4.3 \sqrt{s} distribution of the antibaryon-baryon interactions that lead to the production of a Ξ^- baryon in \bar{p} +Au reactions at $\sqrt{s} = 4$ GeV. Square and circle symbols denote the \sqrt{s} distributions of the $\bar{p} + p \rightarrow \Xi^- + \bar{\Xi}^+ + X$ channel and the $\bar{p} + n \rightarrow \Xi^- + \bar{\Xi}^0 + X$ channel, respectively.

\bar{p} +Au reactions (square) while the average momentum of produced Ξ^- from $\bar{p} + p$ reaction (circle) is approximately 3.4 GeV/c.

4.3 Hyperon induced reactions

In this section, we study how the produced Ξ^- interacts with the secondary target and calculate the fraction of Ξ^- that can be captured in the secondary target.

Shown in Fig. 4.6 are the momentum distributions of Ξ^- after having

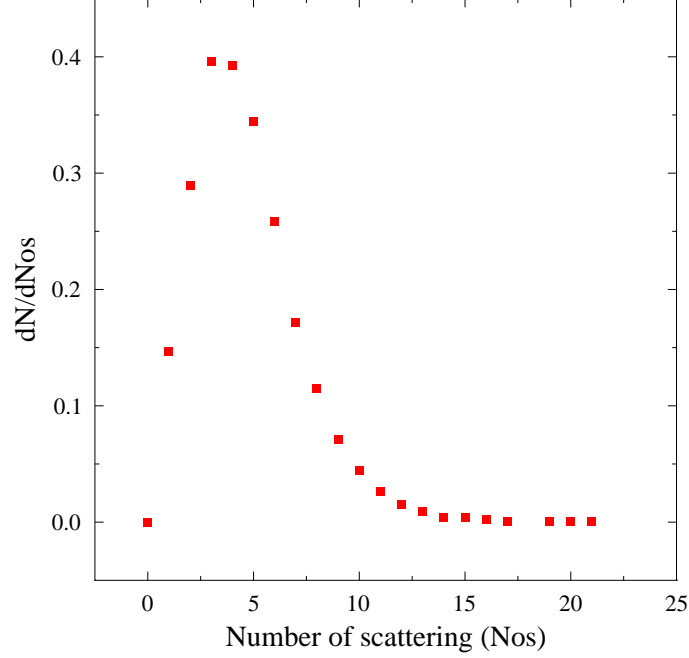


Figure 4.4 Distribution of the number of scatterings (Nos) of the produced Ξ s in $\bar{p}+\text{Au}$ reactions at $\sqrt{s} = 4$ GeV.

reactions with secondary targets Au at incident laboratory momenta from 10 to 300 MeV/c (upper panel) and from 400 to 800 MeV/c (lower panel). Here, the momenta of Ξ^- produced from the first target are selected from Fig. 4.5 and used as the incident laboratory momenta for the secondary reactions $\Xi^- + \text{Au}$. To make sure a secondary reaction may happen one needs to test whether a produced Ξ^- has enough momentum to arrive at the secondary target before it decays. And a Ξ must be stopped/absorbed in the secondary nucleus in order that a hypernucleus is produced. It is found that the Ξ^- particles with laboratory momenta below 20 MeV/c can be totally stopped inside the secondary nucleus. For the Ξ^- with incident momenta between 30 to 100 MeV/c, all of them are slowed down and leave the secondary nucleus with certain values. For example, the Ξ with a momentum

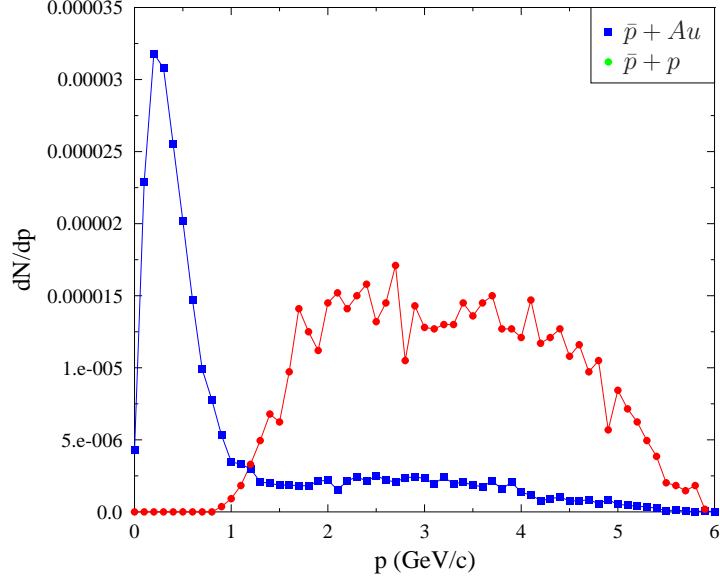


Figure 4.5 Comparison of momentum spectra of the Ξ^- between $\bar{p} + p$ and $\bar{p} + \text{Au}$ reactions at $\sqrt{s} = 4$ GeV. Square symbols denote the data from $\bar{p} + \text{Au}$ reaction, while circle symbols show the data from $\bar{p} + p$ reaction. Here, the momenta are given in the target frame.

100 MeV/c leaves the secondary nucleus with momentum about 40 MeV/c. By comparing to elastic scattering (see appendix D), it is revealed that these Ξ^- are slowed by one time elastic scattering with Au. For Ξ^- particles with initial momenta 200 and 300 MeV/c, one sees two peaks respectively at 90 and 140 MeV/c of Ξ^- , which are clearly resulted from one time elastic scattering. However, the smooth part of the curves for Ξ^- with initial momenta 200 and 300 MeV/c reveals that a fraction of Ξ^- may be scattered many times elastically and/or inelastically before leaving the nucleus with reduced momenta.

Fig. 4.6 (lower panel) shows the momentum distribution of Ξ^- with higher incident momenta, after having reactions with secondary targets Au. It is depicted

that one time elastic scattering which results in the peaks in the momentum distribution, is less important than for the cases with lower incident momenta. With increasing incident momentum, a larger part of Ξ^- is scattered many times elastically and/or inelastically and then leaves the nucleus with reduced momenta.

The Ξ^- which are not stopped in the secondary targets may be stopped by the third targets and so on. The stopping of Ξ^- inside nuclei plays an important role for the hypernucleus production.

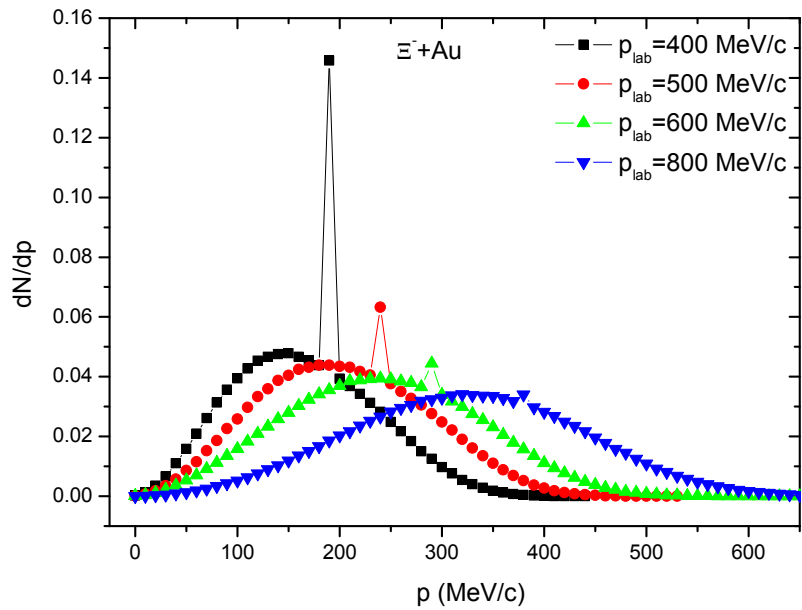
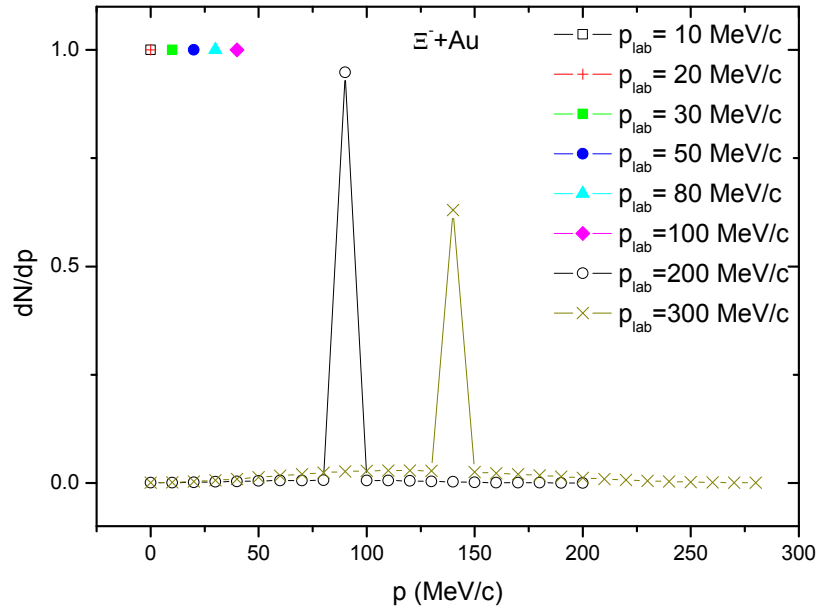


Figure 4.6 Momentum spectra of Ξ^- in $\Xi^- + \text{Au}$ reactions inside the secondary target at laboratory momenta from 10 to 800 MeV/c.

CHAPTER V

SUMMARY

By using the UrQMD model we have calculated the multiplicities of $\Lambda(\Sigma^0)$ and $\bar{\Lambda}(\bar{\Sigma}^0)$ (anti-)hyperons produced in $\bar{p} + A$ collisions at 40 GeV/c and found that the theoretical results are consistent with the experimental data. The UrQMD calculations also reproduce quite well the experimental data for the production of Λ , K^0 and negatively charged hadrons (h^-) in the reaction $\bar{p} + \text{Xe}$ at a \bar{p} momentum of 200 GeV.

The UrQMD calculations reproduce well the experimental data for the transverse momentum distributions of Λ and K^0 and the theoretical results are also in line with the data for the normalized lab rapidity distributions. The positively-skewed curves in Fig. 3.3 for the rapidity distributions of both Λ and K^0 indicate that the particles are mainly produced in the target fragmentation region, and the dominant production of Λ at $y \sim 0$ suggests that a large number of the particles are produced in transverse direction. The UrQMD results on pion production in the reactions $\bar{p} + \text{Mg}$, Ag and Au are found to be consistent with the experimental data, too. Then, we have calculated the multiplicities of hyperons Ξ $\bar{\Xi}$ in different reactions. These predictions are helpful to estimate the trigger conditions in the planned double Λ hypernuclei experiments.

We also have discussed hypernuclei production in anti-proton induced reactions. We find that the multiplicities of K^+K^+ pairs are much higher than the ones of $\bar{\Xi}$ and are comparable to the multiplicities of Ξ , and K^+K^+ pairs can be used as experimental trigger of Ξ productions. The K^+K^+ trigger can be easily

detected at momenta around 0.3 GeV/c. The momenta of Ξ from the $\bar{p}+\text{Au}$ reactions are around 0.2 GeV/c, much lower than the momenta of Ξ from the $\bar{p}+p$ reactions. This implies that the Ξ s are decelerated by re-scattering inside the primary nucleus. The distribution of scattering numbers of produced Ξ reveals that the averaged re-scatterings of Ξ inside the primary nucleus are three times. The decelerated Ξ in the first target may be absorbed or further decelerated inside the secondary nucleus, depending on the momentum. The predictions are relevant for the planned PANDA experiment at FAIR.

REFERENCES

REFERENCES

- Ahn, J. K. et al. (2001). Production of ${}_{\Lambda\Lambda}^4\text{H}$ hypernuclei. **Phys. Rev. Lett.** 87(13): 132504.
- Andersson, B., Gustafson, G., and Sjostrand, T. (1982). A Model for Baryon Production in Quark and Gluon Jets. **Nucl. Phys. B** 197: 45.
- Andersson, B., Gustafson, G., and Soderberg, B. (1983). A General Model for Jet Fragmentation. **Z. Phys. C** 20: 317.
- Aoki, S. et al. (1991). Direct observation of sequential weak decay of a double hypernucleus. **Prog. Theor. Phys.** 85: 1287–1298.
- Barnett, R. M. et al. (1996a). Review of particle physics (Particle Data Group). **Phys. Rev. D** 54: 1–720.
- Barnett, R. M. et al. (1996b). Review of particle physics. Particle Data Group. **Phys. Rev. D** 54: 1–720.
- Bart, S. et al. (1999). Σ hyperons in the nucleus. **Phys. Rev. Lett.** 83: 5238–5241.
- Bass, S. A. et al. (1998). Microscopic models for ultrarelativistic heavy ion collisions. **Prog. Part. Nucl. Phys.** 41: 255–369.
- Bleicher, M. et al. (1999). Relativistic hadron hadron collisions in the ultrarelativistic quantum molecular dynamics model. **J. Phys. G** 25: 1859–1896.
- Bonetti, B. et al. (1954). On the possible ejection of a meson-active triton from a nuclear disintegration. **Il Nuovo Cimento** 11: 210–212.

- Boos, E. G. et al. (1984). Charged particle multiplicities in π^- , K^- and \bar{p} interactions with nuclei at 40 GeV/c. **Z. Phys. C** 26: 43–52.
- Born, K. D., Laermann, E., Sommer, R., Zerwas, P. M., and Walsh, T. F. (1994). The Interquark potential: A QCD lattice analysis. **Phys. Lett. B** 329: 325–331.
- Close, F. E. (1979). Introduction to quark and partons. *Academic Press, London*.
- Danysz, M. et al. (1963a). The identification of a double hyperfragment. **Nuclear Physics** 49: 121–132.
- Danysz, M. et al. (1963b). Observation of a double hyperfragment. **Phys. Rev. Lett.** 11(1): 29–32.
- Danysz, M. and Pniewski, J. (1953). Delayed disintegration of a heavy nuclear fragment. **Philos. Mag.** 44: 348–352.
- Davis, D. H. (1991). Hypernuclei. **Part. Fields** 43: 38. Prepared for Workshop on Strangeness in Nuclei, Cracow, Poland, 5-8 May 1992.
- De Marzo, C. et al. (1982). Multiparticle production on hydrogen, argon and xenon targets in a streamer chamber by 200 GeV/c proton and antiproton beams. **Phys. Rev. D** 26: 1019–1035.
- Derado, I., Kadija, K., Malecki, M., Schmitz, N., and Seyboth, P. (1991). Production of neutral strange particles in p Ar, p Xe and \bar{p} Xe collisions at 200 GeV. **Z. Phys. C** 50: 31–36.
- Dover, C. B. and Gal, A. (1983). Ξ Hypernuclei. **Annals Phys.** 146: 309–348.
- Dover, C. B., Millener, D. J., and Gal, A. (1989). On the production and spectroscopy of sigma hypernuclei. **Phys. Rept.** 184: 1–97.

- Fukuda, T. et al. (1998). Cascade hypernuclei in the (K^-, K^+) reaction on ^{12}C . **Phys. Rev. C** 58: 1306–1309.
- Gal, A. (2005). $\Lambda\Lambda$ hypernuclei and stranger systems. **Nucl. Phys. A** 754: 91–102.
- Galoyan, A. S. and Polanski, A. (2003). Simulation of antiproton nucleus interactions in the framework of the UrQMD model. **hep-ph/0304196**.
- Goulianos, K. (1983). Diffractive Interactions of Hadrons at High-Energies. **Phys. Rept.** 101: 169.
- Grigalashvili, T. et al. (1999). A -dependencies of neutral strange particle yields in \bar{p} nuclei collisions at 40 GeV/c. **Eur. Phys. J. C** 10: 265–270.
- GSI (2001). Conceptual Design Report: An international accelerator facility for beams of ions and antiprotons. <http://www.gsi.de/GSI-Future/cdr>.
- Hayano, R. S. et al. (1989). Observation of a bound state of $^4_{\Sigma}\text{He}$ hypernucleus. **Phys. Lett. B** 231: 355–358.
- Khaustov, P. et al. (2000). Search for double- Λ hypernuclei formation via $(\Xi^-, ^{12}\text{C})_{atom} \rightarrow ^{12}_{\Lambda\Lambda}\text{B} + n$. **Phys. Rev. C** 61: 027601.
- Koch, P. and Dover, C. B. (1989). K^\pm , \bar{p} and Ω^- production in relativistic heavy ion collisions. **Phys. Rev. C** 40: 145–155.
- Kotulla, M. et al. (2004). Strong interaction studies with antiprotons. Letter of intent for PANDA (Antiproton Annihilations at Darmstadt).
- Limphirat, A. et al. (2009). Strange and non-strange particle production in antiproton-nucleus collisions in the UrQMD model. **J. Phys. G** 36: 064049.

- Margaziotis, D. J. (2004). Reactions Some Basics II: Reaction Kinematics. <http://www.calstatela.edu/academic/nuclearphysics/tutorials/djm/kinematics.pdf>.
- Millener, D. J., Dover, C. B., and Gal, A. (1988). Lambda nucleus single particle potentials. **Phys. Rev. C** 38: 2700–2708.
- Nagae, T. et al. (1998). Observation of a ${}^4_{\Sigma}\text{He}$ bound state in the ${}^4\text{He} (K^-, \pi^-)$ reaction at 600 MeV/c. **Phys. Rev. Lett.** 80: 1605–1609.
- Perkin, D. H. (1987). Introduction to high energy physics. *Addison-Wesley*.
- Petersen, H., Bleicher, M., Bass, S. A., and Stocker, H. (2008). UrQMD-2.3 - Changes and Comparisons. **arXiv**: 0805.0567.
- Pochodzalla, J. (2005). Future hypernuclear physics at MAMI-C and PANDA-GSI. **Nucl. Phys. A** 754: 430–442.
- Prowse, D. J. (1966). ${}_{\Lambda\Lambda}{}^6\text{He}$ double hyperfragment. **Phys. Rev. Lett.** 17: 782–785.
- Schwinger, J. S. (1951). On gauge invariance and vacuum polarization. **Phys. Rev.** 82: 664–679.
- Takahashi, H. et al. (2001). Observation of a ${}_{\Lambda\Lambda}{}^6\text{He}$ double hypernucleus. **Phys. Rev. Lett.** 87(21): 212502.
- Tamura, H. et al. (1989). ${}^4_{\Lambda}\text{H}$ formation from K^- absorption at rest on ${}^4\text{He}$, ${}^7\text{Li}$, ${}^9\text{Be}$, ${}^{12}\text{C}$, ${}^{16}\text{O}$ and ${}^{40}\text{Ca}$ targets formation from K^- absorption at rest on ${}^4\text{He}$, ${}^7\text{Li}$, ${}^9\text{Be}$, ${}^{12}\text{C}$, ${}^{16}\text{O}$ and ${}^{40}\text{Ca}$ targets. **Il Nuovo Cimento A** 102: 575–582.
- Tidman, D. A. et al. (1953). Delayed disintegration of a heavy nuclear fragment. **Philos. Mag.** 44: 350.

Whitmore, J. J. et al. (1994). Inclusive charged pion production in hadron nucleus interactions at 100 GeV/c and 320 GeV/c. **Z. Phys. C** 62: 199–227.

Zabrodin, E. E. et al. (1995). Inclusive spectra of charged particles in pp and $\bar{p}p$ interactions at 32 GeV/c. **Phys. Rev. D** 52: 1316–1342.

Zeeb, G., Reiter, M., and Bleicher, M. (2004). Multi-strange baryon production in Au + Au collisions near threshold. **Phys. Lett. B** 586: 297–302.

APPENDICES

APPENDIX A

THE FAIR FACILITIES

The facilities for the FAIR project can be classified into 2 parts: the existing accelerator facility and the new facility. The existing facilities are consist of the universal heavy-ion linear accelerator (UNILAC), the heavy-ion synchrotron (SIS18) and the experimental storage ring (ESR). The briefly characters of these facilities are given below:

- UNILAC is used to delivers beams of heavy-ions and light ions with energies in the range from 3.0 to 13 MeV/u and up to 15 MeV/u respectively,
- SIS18 can be used to accelerated the light ions from energy 100 to 2000 MeV/u, the uranium to 1 GeV/u and proton to 4.7 GeV,
- ESR advantages to accumulate the beams for experiment performance. The ESR is also used to decelerate the beams.

The characters of the new facilities can be shortly described as following below:

- Collector Ring (CR) serves for collecting and stochastic cooling of hot radioactive ion or antiproton beams from production targets.
- New Experimental Storage Ring (NESR) is an accumulator and storage ring for both radioactive ions and antiprotons beam.
- SIS100/SIS200 is served for acceleration the injected antiproton beam, from the NESR, to reach maximum energy of 14 GeV.

- High Energy Storage Ring (HESR) is used to stored antiproton beams, after injected from the SIS100, for experimental performance.
- Super-conducting FRagment Separator (Super-FRS) can be used to increase of radioactive beam intensities by a factor of up to 10,000 and to provide intense antiproton beams, about 15 times higher kinetic energies for heavy-ions.

APPENDIX B

LORENTZ TRANSFORMATION

In this thesis the Lorentz transformation is used to convert between the center of mass (CM) frame and laboratory frame (Lab) when considering the rapidity distribution of Λ and K^0 as seen in chapter III. It is also used to convert the momentum distribution of Ξ^- in chapter IV.

Let start by assuming that there are two observers O and O' , each using their own Cartesian coordinate system to measure space and time intervals. Using coordinate (t, x, y, z) for O and (t', x', y', z') for O' . The velocity v is relative velocity between two observers along the z axis. The Lorentz transform or Lorentz boost in z axis is displayed in the matrix form as:

$$\begin{bmatrix} ct' \\ x' \\ y' \\ z' \end{bmatrix} = \begin{bmatrix} \gamma & 0 & 0 & -\beta\gamma \\ 0 & 1 & 0 & 0 \\ 0 & 0 & 1 & 0 \\ -\beta\gamma & 0 & 0 & \gamma \end{bmatrix} \begin{bmatrix} ct \\ x \\ y \\ z \end{bmatrix} = \begin{bmatrix} \gamma(ct - \beta z) \\ x \\ y \\ \gamma(z - \beta ct) \end{bmatrix} \quad (\text{B.1})$$

where the Lorentz factor $\gamma = \frac{1}{\sqrt{1-\beta^2}}$ and $\beta = \frac{v}{c}$. Substitute the variable β into Eq. (B.1) then we have

$$\begin{aligned} t' &= \gamma \left(t - \frac{vz}{c^2} \right), \\ x' &= x, \\ y' &= y, \\ z' &= \gamma (z - vt). \end{aligned}$$

By the same way, the Lorentz transformation for a 4-vector (E, \vec{p}) can be

written as

$$\begin{bmatrix} E' \\ p'_x \\ p'_y \\ p'_z \end{bmatrix} = \begin{bmatrix} \gamma & 0 & 0 & -\beta\gamma \\ 0 & 1 & 0 & 0 \\ 0 & 0 & 1 & 0 \\ -\beta\gamma & 0 & 0 & \gamma \end{bmatrix} \begin{bmatrix} E \\ p_x \\ p_y \\ p_z \end{bmatrix} = \begin{bmatrix} \gamma(E - \beta p_z) \\ p_x \\ p_y \\ \gamma(p_z - \beta E) \end{bmatrix} \quad (\text{B.2})$$

where the velocity of the particle is $\vec{\beta} = \frac{\vec{p}}{E}$ and $E^2 - |\vec{p}|^2 = m^2$.

APPENDIX C

KINEMATIC VARIABLES

In the field of particle collisions, there are several kinematic variables often used. Let us introduce some of them which appeared in this work. By choosing the z axis as the beam direction, the momentum in z direction is called the longitudinal momentum (p_z). In addition the momentum in perpendicular direction of z axis is transverse momentum (p_t), defined as:

$$p_t = \sqrt{p_x^2 + p_y^2}. \quad (\text{C.1})$$

Also the transverse mass (m_t) can be written in the form

$$m_t = \sqrt{p_t^2 + m^2}. \quad (\text{C.2})$$

Next the method of measuring motion is introduced by the rapidity (y). Rapidity is an alternative to velocity in relativity and proportion to velocity at low speeds. One can be defined as a function of inverse hyperbolic tangent:

$$y = \text{arctanh } \beta, \quad (\text{C.3})$$

where β is velocity.

It can be expanded into

$$y = \beta + \frac{\beta^3}{3} + \dots . \quad (\text{C.4})$$

At small velocity, it is assumed that $y \sim \beta$. One can be rewritten as

$$\begin{aligned}
 \beta &= \tanh y \\
 &= \frac{\sinh y}{\cosh y} \\
 &= \frac{e^y - e^{-y}}{2} \cdot \frac{2}{e^y + e^{-y}} \\
 &= \frac{e^y - e^{-y}}{e^y + e^{-y}} \\
 &= \frac{e^{2y} - 1}{e^{2y} + 1} \\
 e^{2y} &= \frac{1 + \beta}{1 - \beta} \\
 2y &= \ln \frac{1 + \beta}{1 - \beta} \\
 y &= \frac{1}{2} \ln \frac{1 + \beta}{1 - \beta}.
 \end{aligned}$$

The rapidity is also written in the term of energy and longitudinal momentum by inserting the factor γm then we have

$$\begin{aligned}
 y &= \frac{1}{2} \ln \frac{\gamma m + \gamma m \beta}{\gamma m - \gamma m \beta} \\
 &= \frac{1}{2} \ln \frac{E + p_z}{E - p_z}.
 \end{aligned}$$

Moreover the the relation between rapidity, energy, transverse mass and longitudinal momentum can be shown as

$$\begin{aligned}
 y &= \ln \sqrt{\frac{(E + p_z)(E + p_z)}{(E - p_z)(E + p_z)}} = \ln \sqrt{\frac{(E + p_z)^2}{E^2 - p_z^2}} \\
 &= \ln \sqrt{\frac{(E + p_z)^2}{m^2 + p^2 - p_z^2}} = \ln \sqrt{\frac{(E + p_z)^2}{m^2 + p_x^2 + p_y^2 + p_z^2 - p_z^2}} \\
 &= \ln \sqrt{\frac{(E + p_z)^2}{m^2 + p_t^2}} = \ln \sqrt{\frac{(E + p_z)^2}{m_t^2}} \\
 &= \ln \frac{E + p_z}{m_t}.
 \end{aligned}$$

To rewrite energy and p_z in form of hyperbolic cosine and hyperbolic sine,

one needs to start by

$$\begin{aligned}
\cosh y &= \frac{1}{2}(e^y + e^{-y}) \\
&= \frac{1}{2} \left(\frac{E + p_z}{m_t} + \frac{m_t}{E + p_z} \right) \\
&= \frac{E}{m_t} \\
E &= m_t \cosh y
\end{aligned}$$

and

$$\begin{aligned}
\sinh y &= \frac{1}{2}(e^y - e^{-y}) \\
&= \frac{1}{2} \left(\frac{E + p_z}{m_t} - \frac{m_t}{E + p_z} \right) \\
&= \frac{p_z}{m_t} \\
p_z &= m_t \sinh y .
\end{aligned}$$

Consider to Lorentz boosts along the z axis, we have

$$y = \frac{1}{2} \ln \frac{E + p_z}{E - p_z}, \quad (\text{C.5})$$

and

$$y' = \frac{1}{2} \ln \frac{E' + p'_z}{E' - p'_z}, \quad (\text{C.6})$$

where $E' = \gamma(E - \beta p_z)$ and $p'_z = \gamma(p_z - \beta E)$, (see appendix B). Then the relation between y and y' is shown as following below:

$$\begin{aligned}
y' &= \frac{1}{2} \ln \frac{E' + p'_z}{E' - p'_z} \\
&= \frac{1}{2} \ln \frac{\gamma(E - \beta p_z) + \gamma(p_z - \beta E)}{\gamma(E - \beta p_z) - \gamma(p_z - \beta E)} \\
&= \frac{1}{2} \ln \frac{(E + p_z)(1 - \beta)}{(E - p_z)(1 + \beta)} \\
&= \frac{1}{2} \ln \frac{E + p_z}{E - p_z} + \frac{1}{2} \ln \frac{1 - \beta}{1 + \beta} \\
&= y - y_{\text{boost}} .
\end{aligned}$$

APPENDIX D

TWO-BODY ELASTIC SCATTERING

There are many different reactions for the scattering of an incident beam on a target. For example the elastic and inelastic scattering are represented by different collisions of beam particles with different nuclei. To identify the particles involved with correct energy and direction, the kinematics of the reaction are useful. The two-body kinematics are used when two particles are present in the final state.

Fig. D.1 shows that the incident beam of a particle with mass m_1 , momentum \vec{p}_1 and kinetic energy K_1 is scattering off a target with mass m_2 and $\vec{p}_2=0$, $K_2=0$. After scattering, the particle m_1 has the momentum \vec{p}'_1 , kinetic energy K'_1 and angle θ'_1 with the incident direction. While the particle m_2 has the momentum \vec{p}'_2 , kinetic energy K'_2 and angle θ'_2 with the incident direction.

Due to the conservation of energy, we have

$$E_1 + m_2 = E'_1 + E'_2 \quad (\text{D.1})$$

where

$$\begin{aligned} E_1^2 &= p_1^2 + m_1^2, \\ E'^2_1 &= p'^2_1 + m_1^2, \\ E'^2_2 &= p'^2_2 + m_2^2. \end{aligned}$$

For conservation of momentum, we have

$$p_1 = p'_1 \cos\theta'_1 + p'_2 \cos\theta'_2 \quad (\text{D.2})$$

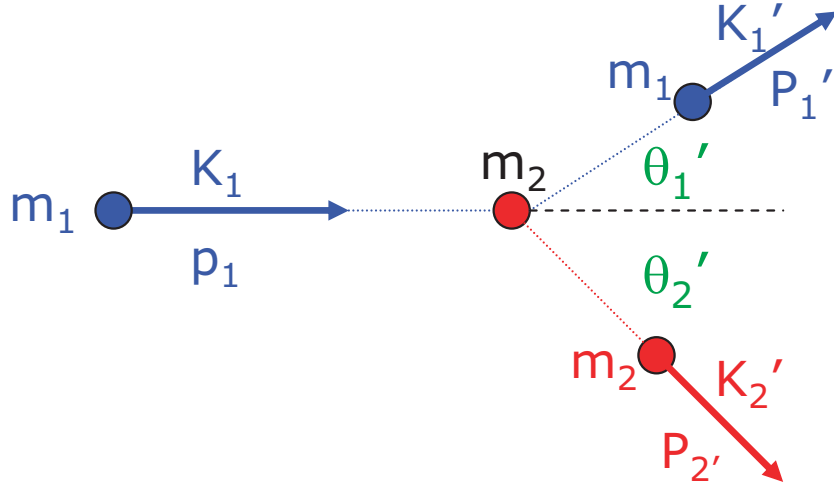


Figure D.1 Two-body scattering.

and

$$0 = p'_1 \sin \theta'_1 - p'_2 \sin \theta'_2. \quad (\text{D.3})$$

Next the Eq. (D.1), (D.2) and (D.3) are solved by using

$$E_1 = K_1 + m_1,$$

$$E'_1 = K'_1 + m_1,$$

$$E'_2 = K'_2 + m_2.$$

Finally, we get

$$E'_1 = \frac{A_1(E_1 + m_1) \pm p_1 \cos \theta'_1 \sqrt{A_1^2 - 4m_1^2[(E_1 + m_2)^2 - p_1^2 \cos^2 \theta'_1]}}{2[(E_1 + m_2)^2 - p_1^2 \cos^2 \theta'_1]}, \quad (\text{D.4})$$

$$E'_2 = \frac{A_2(E_1 + m_2) \pm p_1 \cos \theta'_2 \sqrt{A_2^2 - 4m_2^2[(E_1 + m_2)^2 - p_1^2 \cos^2 \theta'_2]}}{2[(E_1 + m_2)^2 - p_1^2 \cos^2 \theta'_2]}, \quad (\text{D.5})$$

$$\cot \theta'_2 = \frac{-(1 + \rho_1 \rho_2) \cot \theta'_1 \pm (\rho_1 + \rho_2) \sqrt{\gamma^2(1 - \rho_1^2) + \cot^2 \theta'_1}}{1 - \rho_1^2}. \quad (\text{D.6})$$

The parameters A_1, A_2, ρ_1, ρ_2 and γ are represented by

$$\begin{aligned}
 A_1 &= 2(m_1^2 + m_1 m_2 + m_2 K_1), \\
 A_2 &= 2(m_2^2 + m_1 m_2 + m_2 K_1), \\
 \rho_1 &= \frac{A_1 p_1}{(E_1 + m_2) \sqrt{A_1^2 - 4m_1^2[(E_1 + m_2)^2 - p_1^2]}}, \\
 \rho_2 &= \frac{A_2 p_1}{(E_1 + m_2) \sqrt{A_2^2 - 4m_2^2[(E_1 + m_2)^2 - p_1^2]}}, \\
 \gamma &= \frac{E_1 + m_2}{m_1^2 + m_2(2E_1 + m_2)}.
 \end{aligned}$$

For more detail, one can see in Ref. (Margaziotis, 2004).

APPENDIX E

THERMAL DISTRIBUTION

The elementary processes lead to statistical/thermal particle production, that means, the thermodynamics can be applied to calculate the particle spectra and yields (multiplicities). Within this appendix we are focusing on the yields. Let us start with the phase space density:

$$\frac{d^6 N}{d^3 p d^3 x} = \frac{g}{(2\pi)^3} e^{-(E-\mu)/T}, \quad (\text{E.1})$$

where

- g is degeneracy factor
- T is temperature
- μ is chemical potential
- E is energy ($E^2 = p^2 + m^2$).

Then the phase space density is integrated over space, we have

$$\frac{d^3 N}{d^3 p} = \frac{gV}{(2\pi)^3} e^{-(E-\mu)/T}, \quad (\text{E.2})$$

where V is volume. Next it is integrated over momentum,

$$\begin{aligned} N &= \frac{gV}{(2\pi)^3} \int d^3 p e^{-(E-\mu)/T} \\ &= \frac{gV e^{\mu/T}}{(2\pi)^3} \int d^3 p e^{-E/T} \\ &= \frac{gV e^{\mu/T}}{(2\pi)^3} \int \int \int dp_x dp_y dp_z e^{-E/T}. \end{aligned}$$

Let change the variables (p_x, p_y, p_z) to (y, m_t, ϕ) by

$$p_t = \sqrt{p_x^2 + p_y^2} ,$$

$$\frac{p_y}{p_x} = \tan\phi ,$$

and

$$p_x = p_t \cos\phi ,$$

$$p_y = p_t \sin\phi .$$

From appendix C:

$$p_z = m_t \sinh y .$$

Now, we have

$$p_x = p_t \cos\phi ,$$

$$p_y = p_t \sin\phi ,$$

$$p_z = m_t \sinh y .$$

Substitute $p_t = \sqrt{m_t^2 - m^2}$ into above equations, we get

$$p_x = \sqrt{m_t^2 - m^2} \cos\phi ,$$

$$p_y = \sqrt{m_t^2 - m^2} \sin\phi ,$$

$$p_z = m_t \sinh y .$$

Then the above relations are differentiated:

$$dp_x = \cos\phi \frac{m_t}{\sqrt{m_t^2 - m^2}} dm_t - \sqrt{m_t^2 - m^2} \sin\phi d\phi ,$$

$$dp_y = \sin\phi \frac{m_t}{\sqrt{m_t^2 - m^2}} dm_t + \sqrt{m_t^2 - m^2} \cos\phi d\phi ,$$

$$dp_z = \sinh y dm_t + m_t \cosh y dy .$$

Here the energy E is written in the terms of rapidity and transverse mass, we have

$$E = m_t \cosh y .$$

The 3-dimensional measured in momentum space :

$$d^3p \equiv dp_x dp_y dp_z = \left| \frac{\partial(p_x, p_y, p_z)}{\partial(m_t, y, \phi)} \right| dm_t dy d\phi , \quad (\text{E.3})$$

where the Jacobian $\frac{\partial(p_x, p_y, p_z)}{\partial(m_t, y, \phi)}$ is defined by the determinant

$$\frac{\partial(p_x, p_y, p_z)}{\partial(m_t, y, \phi)} \equiv \begin{vmatrix} \frac{\partial p_x}{\partial m_t} & \frac{\partial p_y}{\partial m_t} & \frac{\partial p_z}{\partial m_t} \\ \frac{\partial p_x}{\partial y} & \frac{\partial p_y}{\partial y} & \frac{\partial p_z}{\partial y} \\ \frac{\partial p_x}{\partial \phi} & \frac{\partial p_y}{\partial \phi} & \frac{\partial p_z}{\partial \phi} \end{vmatrix} \quad (\text{E.4})$$

$$= \begin{vmatrix} \frac{m_t \cos \phi}{\sqrt{m_t^2 - m^2}} & \frac{m_t \sin \phi}{\sqrt{m_t^2 - m^2}} & \sinh y \\ 0 & 0 & m_t \cosh y \\ -\sqrt{m_t^2 - m^2} \sin \phi & \sqrt{m_t^2 - m^2} \cos \phi & 0 \end{vmatrix}$$

$$= -m_t^2 \cosh y . \quad (\text{E.5})$$

Therefore $\left| \frac{\partial(p_x, p_y, p_z)}{\partial(m_t, y, \phi)} \right| = m_t^2 \cosh y = E m_t$, then

$$d^3p = E m_t dm_t dy d\phi .$$

The integral become to

$$\begin{aligned} N &= \frac{gV e^{\mu/T}}{(2\pi)^3} \int d^3p e^{-E/T} \\ &= \frac{gV e^{\mu/T}}{(2\pi)^3} \int_{y=-\infty}^{\infty} \int_{m_t=m}^{\infty} \int_{\phi=0}^{2\pi} e^{-E/T} E m_t d\phi dm_t dy, \end{aligned}$$

and use $E = m_t \cosh y$, we get

$$\begin{aligned}
N &= \frac{gV e^{\mu/T}}{(2\pi)^3} \int_{y=-\infty}^{\infty} \int_{m_t=m}^{\infty} \int_{\phi=0}^{2\pi} e^{-m_t \cosh y/T} m_t^2 \cosh y d\phi dm_t dy \\
&= \frac{gV e^{\mu/T}}{(2\pi)^2} \int_{y=-\infty}^{\infty} \int_{m_t=m}^{\infty} e^{-m_t \cosh y/T} m_t^2 \cosh y dm_t dy \\
&= \frac{gV e^{\mu/T}}{(2\pi)^2} \int_{y=-\infty}^{\infty} e^{-m \cosh y/T} \frac{T}{\cosh^2 y} [2T^2 + 2mT \cosh y + m^2 \cosh^2 y] dy \\
&= \frac{gVT^3 e^{\mu/T}}{(2\pi)^2} \int_{y=-\infty}^{\infty} e^{-m \cosh y/T} \left[\frac{2}{\cosh^2 y} + \frac{2m}{T \cosh y} + \frac{m^2}{T^2} \right] dy.
\end{aligned}$$

Because of the cosh is the even function, so

$$N = \frac{gVT^3 e^{\mu/T}}{(2\pi)^2} 2 \int_{y=0}^{\infty} e^{-m \cosh y/T} \left[\frac{2}{\cosh^2 y} + \frac{2m}{T \cosh y} + \frac{m^2}{T^2} \right] dy. \quad (\text{E.6})$$

Next substitute $z = \frac{m}{T}$ into Eq. (E.6), we have

$$N = \frac{gVT^3 e^{\mu/T}}{2\pi^2} \left[\int_0^{\infty} dy e^{-z \cosh y} \left(\frac{2}{\cosh^2 y} + \frac{2z}{\cosh y} + z^2 \right) \right]. \quad (\text{E.7})$$

The integral is represented for the modified Bessel function of the second kind:

$$K_v(z) = \int_0^{\infty} dy e^{-z \cosh y} \cosh(vy),$$

where $\text{Re}(z) > 0$.

Consider:

$$\begin{aligned}
A(z) &= \int_0^{\infty} dy e^{-z \cosh y} \left(\frac{2}{\cosh^2 y} + \frac{2z}{\cosh y} + z^2 \right), \\
A(0) &= \int_0^{\infty} dy \frac{2}{\cosh^2 y} = 2,
\end{aligned}$$

$$\begin{aligned}
\frac{dA(z)}{dz} &= \int_0^{\infty} dy \frac{\partial}{\partial z} \left[e^{-z \cosh y} \left(\frac{2}{\cosh^2 y} + \frac{2z}{\cosh y} + z^2 \right) \right] \\
&= \int_0^{\infty} dy [-z^2 \cosh y e^{-z \cosh y}] \\
&= -z^2 \underbrace{\int_0^{\infty} dy e^{-z \cosh y} \cosh y}_{K_1(z)} \\
&= -z^2 K_1(z),
\end{aligned}$$

and

$$\begin{aligned}
\int_0^z dA(t) &= - \int_0^z t^2 K_1(t) dt \\
A(z) - A(0) &= - \int_0^z t^2 K_1(t) dt \\
A(z) &= A(0) - \int_0^z t^2 K_1(t) dt.
\end{aligned}$$

The relation as following below can be used

$$\frac{d}{dz} [z^v K_v(z)] = -z^v K_{v-1}(z)$$

with $v = 2$, we get

$$\begin{aligned}
\frac{d}{dt} [t^2 K_2(t)] &= -t^2 K_1(t) \\
\int_0^z d [t^2 K_2(t)] &= - \int_0^z t^2 K_1(t) dt \\
z^2 K_2(z) - 2 &= - \int_0^z t^2 K_1(t) dt,
\end{aligned}$$

where $\lim_{t \rightarrow 0} [t^2 K_2(t)] = 2$ as seen in Fig. E.1.

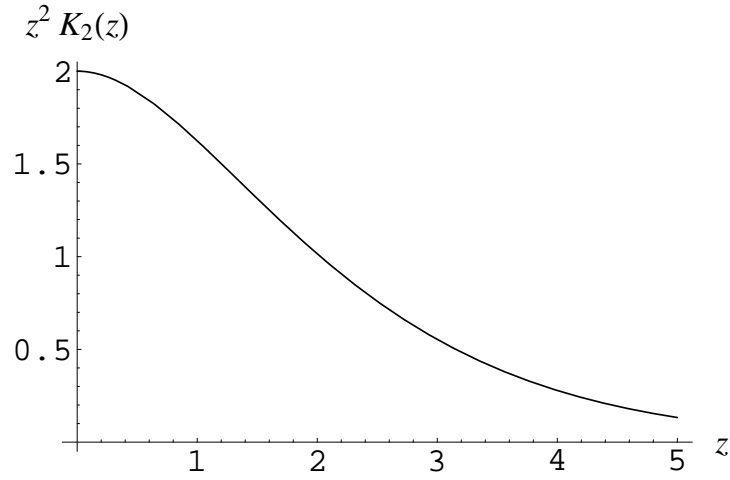


Figure E.1 Limit of $z^2 K_2(z)$ when $z \rightarrow 0$.

Now we get

$$\begin{aligned}
 A(z) &= A(0) - \int_0^z t^2 K_1(t) dt \\
 &= 2 + z^2 K_2(z) - 2 \\
 &= z^2 K_2(z).
 \end{aligned}$$

Substitute $A(z)$ into Eq. (E.7), we get

$$\begin{aligned}
 N &= \frac{gVT^3 e^{\mu/T}}{2\pi^2} \underbrace{\left[\int_0^\infty dy e^{-z \cosh y} \left(\frac{2}{\cosh^2 y} + \frac{2z}{\cosh y} + z^2 \right) \right]}_{A(z)=z^2 K_2(z)} \\
 &= \frac{gVT^3 e^{\mu/T}}{2\pi^2} z^2 K_2(z) \\
 &= \frac{gVT^3 e^{\mu/T}}{2\pi^2} \frac{m^2}{T^2} K_2\left(\frac{m}{T}\right).
 \end{aligned}$$

Case: $m \ll T$

$$\begin{aligned}
 \frac{m^2}{T^2} K_2\left(\frac{m}{T}\right) &\rightarrow 2, \\
 N &= \frac{gVT^3 e^{\mu/T}}{\pi^2}.
 \end{aligned}$$

Case: $m \gg T$

$$K_\nu(z \gg |v^2 - 1/4|) \rightarrow \sqrt{\frac{\pi}{2z}} e^{-z},$$

$$K_2\left(\frac{m}{T}\right) \xrightarrow{m \gg T} \sqrt{\frac{\pi T}{2m}} e^{-m/T}.$$

Finally we get the particle yields as shown in this form

$$N = \frac{gV e^{\mu/T}}{2\pi^2} T^{3/2} m^{3/2} \sqrt{\frac{\pi}{2}} e^{-m/T}.$$

Note that some details can be proved as following below.

Proof 1:

$$\frac{d}{dz} [z^v K_v(z)] = -z^v K_{v-1}(z)$$

$$\begin{aligned} K_v(z) &= \int_0^\infty dy e^{-z \cosh y} \cosh(vy) \\ z^v K_v(z) &= \int_0^\infty dy z^v e^{-z \cosh y} \cosh(vy) \\ \frac{d}{dz} [z^v K_v(z)] &= \int_0^\infty dy \cosh(vy) \frac{d}{dz} [z^v e^{-z \cosh y}] \\ &= \int_0^\infty dy \cosh(vy) [-\cosh y z^v e^{-z \cosh y} + v z^{v-1} e^{-z \cosh y}] \\ &= \int_0^\infty dy \cosh(vy) e^{-z \cosh y} [-\cosh y z^v + v z^{v-1}] \\ &= v z^{v-1} \underbrace{\int_0^\infty dy \cosh(vy) e^{-z \cosh y}}_{K_v(z)} - z^v \int_0^\infty dy \cosh(vy) e^{-z \cosh y} \cosh y \\ &= v z^{v-1} K_v(z) - z^v \int_0^\infty dy e^{-z \cosh y} \frac{1}{2} [\cosh(v+1)y + \cosh(v-1)y] \end{aligned}$$

$$\begin{aligned}
&= vz^{v-1}K_v(z) \\
&\quad - \frac{z^v}{2} \left[\underbrace{\int_0^\infty dy e^{-z \cosh y} \cosh(v+1)y}_{K_{v+1}(z)} + \underbrace{\int_0^\infty dy e^{-z \cosh y} \cosh(v-1)y}_{K_{v-1}(z)} \right] \\
&= vz^{v-1}K_v(z) - \frac{z^v}{2} [K_{v+1}(z) + K_{v-1}(z)] \\
&= \frac{z^v}{2} \left[\underbrace{\frac{2v}{z}K_v(z) - K_{v+1}(z) - K_{v-1}(z)}_{-K_{v-1}(z)} \right] \\
\frac{d}{dz} [z^v K_v(z)] &= -z^v K_{v-1}(z)
\end{aligned}$$

Proof 2:

$$K_{v+1}(z) - K_{v-1}(z) = \frac{2v}{z}K_v(z)$$

$$\begin{aligned}
K_{v+1}(z) - K_{v-1}(z) &= \int_0^\infty dy e^{-z \cosh y} \cosh(v+1)y - \int_0^\infty dy e^{-z \cosh y} \cosh(v-1)y \\
&= \int_0^\infty dy e^{-z \cosh y} \underbrace{[\cosh(v+1)y - \cosh(v-1)y]}_{2 \sinh y \sinh(vy)} \\
&= 2 \int_0^\infty dy e^{-z \cosh y} \sinh y \sinh(vy) \\
&= 2 \int_{y=0}^\infty d(\cosh y) e^{-z \cosh y} \sinh(vy) \\
&= -\frac{2}{z} \int_{y=0}^\infty d(e^{-z \cosh y}) \sinh(vy)
\end{aligned}$$

$$\begin{aligned}
&= -\frac{2}{z} \left\{ \underbrace{\left[e^{-z \cosh y} \sinh(vy) \right]_{y=0}^{\infty}}_0 - \int_{y=0}^{\infty} d(\sinh(vy)) e^{-z \cosh y} \right\} \\
&= \frac{2v}{z} \underbrace{\int_{y=0}^{\infty} dy e^{-z \cosh y} \cosh(vy)}_{K_v(z)}
\end{aligned}$$

$$K_{v+1}(z) - K_{v-1}(z) = \frac{2v}{z} K_v(z)$$

APPENDIX F

DATA ANALYSIS SCRIPT

In this appendix the script files which used to analyze our output data, are displayed. Here the script files are written in the format of PERL language.

F.1 Multiplicity analysis script

To read the multiplicity of Ξ s from the output data, the script are shown as following below:

```
#!/usr/bin/perl
#####
#
# read data of Xi- (multiplicity)
#
#####
$numfile=50;
$name='au_pbarAu_ecm4.0_';
for ($zz=1; $zz<=$numfile; $zz++){
open(INFILE, $name.$zz.".f14");
while(<INFILE>) {
    @stuff=split(' ');
    if(/UQMD/){
    }
    elsif(/projectile:/){
```

```
$protar=$_  
}  
elif(/transformation/){  
    $beta=$stuff[4];  
}  
elif(/equation_of_state:/){  
    $ecm=$stuff[5];  
    $midy=log($ecm/0.938);  
    $elab=$stuff[3];  
    $plab=$stuff[7];  
}  
elif(/event#/){  
    $noe++  
}  
else{  
    if($#stuff==14||$#stuff==13){  
        @x=@stuff[0..3];  
        @p=@stuff[4..7];  
        @id=@stuff[8..13];  
        $mass=$id[0];  
        $ityp=$id[1];  
        $iz2=$id[2];  
        $charge=$id[3];  
        $nocolli=$id[5];  
        if ($ityp==49 && $charge==-1){  
            $countxim++;  
        }  
    }  
}
```

```

}
if ($ityp==49 && $charge==0){
    $countxi0++;
}
if ($ityp==-49 && $charge==1){
    $countximbar++;
}
if ($ityp==-49 && $charge==0){
    $countxi0bar++;
}
}
}
}
}
close INFILE;
}
open(OUTFILE, ">mulxi_".$iname."2.dat");
print OUTFILE "multiplicity for Xi \n";
print OUTFILE "Xi- Xi0 Xi-bar Xi0bar \n";
print OUTFILE $countxim/$noe," ",$countxi0/$noe," ",
    $countximbar/$noe," ",$countxi0bar/$noe,"\n";

```

F.2 Transverse momentum analysis script

This script is used to plot the transverse momentum distribution.

```

#!/usr/bin/perl
#####
#

```

```

### To calculate transverse momentum
### 1/N 1/pt dN/dpt
#
#####
$dpt=.1;
$numfile=1;
$iname='pbarA200_b_pbarXe_plb200_';
for ($zz=1; $zz<=$numfile; $zz++){
open(INFILE, $iname.$zz.".f14");
while(<INFILE>) {
  @stuff=split(' ');
  if(/UQMD/){
  }
  elsif(/projectile:/){
    $protar=$_
  }
  elsif(/equation_of_state:/){
  }
  elsif(/event#/){
    $noe++
  }
  else{
    if($#stuff==14 | $#stuff==13){
      @x=@stuff[0..3];
      @p=@stuff[4..7];
      @id=@stuff[8..13];

```

```

$mass=$id[0];
$ityp=$id[1];
$iz2=$id[2];
$charge=$id[3];
$nocl=$id[5];
if ($ityp==27 && $charge==0){
    $pt2pip=sqrt($p[1]*$p[1]+$p[2]*$p[2]);
    $iptpip=int($pt2pip/$dpt);
    $npip[$iptpip]++;
}
if ($ityp==106 && $charge==0){
    $pt2pim=sqrt($p[1]*$p[1]+$p[2]*$p[2]);
    $iptpim=int($pt2pim/$dpt);
    $npim[$iptpim]++;
}
}
}
}
close INFILE;
}
open(OUTFILE1, ">dndptlambda_".$iname.".dat");
print OUTFILE1 "! p_t , 1/N dN/dpt \n";
foreach $i(0 .. $#npip){
    print OUTFILE1 $i*$dpt+$dpt/2," ",
        $npip[$i]/$dpt/$noe/($i*$dpt+$dpt/2)," \n";
}

```

```

open(OUTFILE2, ">dndptk0_".$iname.".dat");
print OUTFILE2 "! p_t , 1/N dN/dpt \n";
foreach $i(0 .. $#npim){
    print OUTFILE2 $i*$dpt+$dpt/2," ",
        $npim[$i]/$dpt/$noe/($i*$dpt+$dpt/2),"\n";
}

```

F.3 Rapidity analysis script

For rapidity distribution, the following script below is useful.

```

#!/usr/bin/perl
#####
#
###   To calculate   rapidity
###   1/N dN/dy
#
#####
$dy=.1;
$numfile=1;
$iname='pbarA1_pbarAu_plb100_';
for ($zz=1; $zz<=$numfile; $zz++){
open(INFILE, $iname.$zz.".f14");
while(<INFILE>) {
    @stuff=split(' ');
    if(/UQMD/){
    }
    elsif(/projectile:){

```

```

$protar=$_
}
elseif(/transformation/){
    $beta=$stuff[4];
    $gam=1/sqrt(1-$beta*$beta);
}
elseif(/equation_of_state:/){
}
elseif(/event#/){
    $noe++
}
else{
    if($#stuff==14 | $#stuff==13){
        @x=@stuff[0..3];
        @p=@stuff[4..7];
        @id=@stuff[8..13];
        $mass=$id[0];
        $ityp=$id[1];
        $iz2=$id[2];
        $charge=$id[3];
        $nocl=$id[5];
        if ($ityp==101 && $charge==1){
            $ypip=(0.5*log(($p[0]+$p[3])/($p[0]-$p[3])))
                +(0.5*log((1+$beta)/(1-$beta)));
            $yminpip=-10;
            $iypip=int(($ypip-$yminpip)/$dy);

```

```

    $npip[$iypip]++;
}
if ($ityp==101 && $charge==-1){
    $ypim=(0.5*log(($p[0]+$p[3])/($p[0]-$p[3])))
        +(0.5*log((1+$beta)/(1-$beta)));
    $yminpip=-10;
    $iypim=int(($ypim-$yminpip)/$dy);
    $npim[$iypim]++;
}
}
}
}
}
close INFILE;
}
open(OUTFILE1, ">dndypip_".$inname.".dat");
print OUTFILE1 "! y , 1/N dN/dy \n";
foreach $i(0 .. $#npip){
    print OUTFILE1 $i*$dy+$dy/2+$yminpip, " ", $npip[$i]/$dy/$noe, "\n";
}
open(OUTFILE2, ">dndypim_".$inname.".dat");
print OUTFILE2 "! y , 1/N dN/dy \n";
foreach $i(0 .. $#npim){
    print OUTFILE2 $i*$dy+$dy/2+$yminpip, " ", $npim[$i]/$dy/$noe, "\n";
}
}

```

F.4 Analysis script for read the data of Ξ^-

In case of several output files, we can read only the important data by using the script here.

```
#!/usr/bin/perl

#####

#

# read data of Xi-

#

#####

$numfile=200;

$iname='xi_pbarp_ecm4.0_';

for ($zz=1; $zz<=$numfile; $zz++){

open(INFILE, $iname.$zz.".f14");

while(<INFILE>) {

    @stuff=split(' ');

    if(/UQMD/){

    }

    elsif(/projectile:/){

        $protar=$_

    }

    elsif(/transformation/){

        $beta=$stuff[4];

    }

    elsif(/equation_of_state:/){

        $ecm=$stuff[5];

        $midy=log($ecm/0.938);

    }

}

}
```

```
$elab=$stuff[3];
$plab=$stuff[7];
}
elseif(/event#/){
  $noe++
}
else{
  if($#stuff==14||$#stuff==13){
    @x=@stuff[0..3];
    @p=@stuff[4..7];
    @id=@stuff[8..13];
    $mass=$id[0];
    $ityp=$id[1];
    $iz2=$id[2];
    $charge=$id[3];
    $nocolli=$id[5];
    if ($ityp==49 && $charge==-1){
      $count++;
      $px[$count]=$p[1];
      $py[$count]=$p[2];
      $pz[$count]=$p[3];
      $En[$count]=$p[0];
      $beta1[$count]=$beta;
      $nocol[$count]=$nocolli;
    }
  }
}
```

```

}
}
close INFILE;
}

open(OUTFILE, ">dataxi_".$inname."3.dat");
print OUTFILE "noe: ",$noe,"\n";
print OUTFILE "beta_E_px_py_pz \n";
foreach $i(1 .. $count){
    print OUTFILE $beta1[$i]," ",$En[$i]," ",$px[$i]," ",
                $py[$i]," ",$pz[$i]," ",$nocol[$i]," \n";
}

```

F.5 Scattering number analysis script

This script provides the number of scattering of Ξ^- .

```

#!/usr/bin/perl

#####

#

# no of collision distribution of Xi-

# dn/dnoc(xi-) vs noc(xi-)

#

#####

$dnc=.1;

$numfile=4;

$inname='dataxi_au_pbarAu_ecm3.0_';

for ($zz=1; $zz<=$numfile; $zz++){

open(INFILE, $inname.$zz.".dat");

```

```

while(<INFILE>) {
  @stuff=split(' ');
  if(/noe:/{
    $noev[$zz]=$stuff[1];
    $noe=$noe+$noev[$zz];
  }
  else{
    if($#stuff==4||$#stuff==5){
      @xx=@stuff[0..5];
      #$xx[0] = beta
      #$xx[1] = Energy
      #$xx[2] = px
      #$xx[3] = py
      #$xx[4] = pz
      #$xx[5] = no of collision
      $nxi=$xx[5];
      $inxi=int($nxi/$dnc);
      $n[$inxi]++;
    }
  }
}
close INFILE;
}
open(OUTFILE, ">nocoll_".$inname.".dat");
print OUTFILE "! noc , dN/dnoc \n";
foreach $i(0 .. $#n){

```

```

print OUTFILE $i*$dnc+$dnc/2," ",$n[$i]/$dnc/$noe,"\n";
}

```

F.6 Momentum distribution analysis script

The following script below is used to analyze the momentum distribution of Ξ^- .

```

#!/usr/bin/perl
#####
#
# momentum distribution of Xi-
# dn/dp(xi-) vs p(xi-)
# LaB Frame
#
#####
$dpt=.01;
$numfile=1;
$iname='XiAu_xiAu_plb0.03_';
for ($zz=1; $zz<=$numfile; $zz++){
open(INFILE, $iname.$zz.".f14");
while(<INFILE>) {
    @stuff=split(' ');
    if(/UQMD/){
    }
    elsif(/projectile:/){
        $protar=$_
    }
}

```

```
elseif(/transformation/){
    $beta=$stuff[4];
    $gam=1/sqrt(1-$beta*$beta);
}
elseif(/equation_of_state:/){
    $ecm=$stuff[5];
    $midy=log($ecm/0.938);
    $elab=$stuff[3];
    $plab=$stuff[7];
}
elseif(/event#/){
    $noe++
}
else{
    if($#stuff==14||$#stuff==13){
        @x=@stuff[0..3];
        @p=@stuff[4..7];
        @id=@stuff[8..11];

        $mass=$id[0];
        $ityp=$id[1];
        $iz2=$id[2];
        $charge=$id[3];

        if ($ityp==49 && $charge==-1){
            $pzp=$gam*($p[3]+$beta*$p[0]);
```

```
$pxi=sqrt($p[1]*$p[1]+$p[2]*$p[2]+$pzp*$pzp);
$ipxi=int($pxi/$dpt);
$n[$ipxi]++;
$nall++;
}
}
}
}
close INFILE;
}
open(OUTFILE, ">labmom_".$inname.".dat");
print OUTFILE "! p_xi , dN/dpxi \n";
print OUTFILE "! ",$protar,"\n";
foreach $i(0 .. $#n){
print OUTFILE $i*$dpt+$dpt/2," ",$n[$i]/$dpt/$noe/$nall,"\n";
}
}
```

APPENDIX G
PUBLICATION PAPER

Strange and non-strange particle production in antiproton–nucleus collisions in the UrQMD model

Ayut Limphirat¹, Chinorat Kobdaj¹, Marcus Bleicher², Yupeng Yan¹
and Horst Stöcker^{2,3,4}

¹ School of Physics, Suranaree University of Technology, Nakhon Ratchasima 30000, Thailand

² Institut für Theoretische Physik, Johann Wolfgang Goethe-Universität, Max-von-Laue-Str 1, 60438 Frankfurt am Main, Germany

³ Frankfurt Institute for Advanced Studies (FIAS), Johann Wolfgang Goethe-Universität, Ruth-Moufang-Str 1, 60438 Frankfurt am Main, Germany

⁴ GSI Helmholtzzentrum für Schwerionenforschung, Planckstr 1, 64291 Darmstadt, Germany

E-mail: limphirat@yahoo.com

Received 7 January 2009

Published 13 May 2009

Online at stacks.iop.org/JPhysG/36/064049

Abstract

The capabilities of the ultra-relativistic quantum molecular dynamics (UrQMD) model in describing antiproton–nucleus collisions are presented. The model provides a good description of the experimental data on multiplicities, transverse momentum distributions and rapidity distributions in antiproton–nucleus collisions. Special emphasis is put on the comparison of strange particles in reactions with nuclear targets ranging from ${}^7\text{Li}$, ${}^{12}\text{C}$, ${}^{32}\text{S}$, ${}^{64}\text{Cu}$ to ${}^{131}\text{Xe}$ because of the important role of strangeness for the exploration of hypernuclei at PANDA-FAIR. The productions of the double strange baryons Ξ^- and $\bar{\Xi}^+$, which may be used to produce double Λ hypernuclei, are predicted in this work for the reactions $\bar{p} + {}^{24}\text{Mg}$, ${}^{64}\text{Cu}$ and ${}^{197}\text{Au}$.

1. Introduction

Quantum chromodynamics (QCD) is the well-accepted theory to describe the physics of strong interaction. However, for low and medium energy reactions where the distance scale is on the order of $1/\Lambda_{\text{QCD}}$, interactions among quarks and gluons become so strong ($\alpha_s \sim 0.1$) [1] that perturbative methods cannot be applied anymore and one has to deal with QCD in non-perturbative approaches. Aiming at the exploration of the non-perturbative features of QCD antiproton annihilations on nuclear targets will be performed by the PANDA (antiProton ANihilation at Darmstadt) experiment at the currently built Facility for Antiproton and Ion Research (FAIR) [2].

The investigation of double Λ hypernuclei is one of the major physics topics of PANDA together with the exploration of exotic charm and gluon states. The production of double Λ

Table 1. Comparison between experimental data [7] and UrQMD results for the average multiplicities of $\Lambda(\Sigma^0)$ and $\bar{\Lambda}(\bar{\Sigma}^0)$.

Target	$\langle n_{\Lambda(\Sigma^0)} \rangle$		$\langle n_{\bar{\Lambda}(\bar{\Sigma}^0)} \rangle$	
	Experimental	UrQMD	Experimental	UrQMD
Li	0.07 ± 0.01	0.06	0.06 ± 0.01	0.05
C	0.08 ± 0.02	0.07	0.06 ± 0.02	0.06
S	0.13 ± 0.01	0.11	0.07 ± 0.01	0.06
Cu	0.15 ± 0.02	0.17	0.05 ± 0.02	0.06

hypernuclei is based on the capture reaction $\Xi^- + p \rightarrow \Lambda \Lambda$, where the initial hyperon pair $\Xi \bar{\Xi}$ can be produced in a primary antiproton+nucleus interaction [3]. In this work, we set the stage for further studies of hypernuclei by exploring the production rates of strange and non-strange particles in antiproton–nucleus collisions. The paper is arranged as follows: in section 2, we employ the ultra-relativistic quantum molecular dynamics (UrQMD) model to calculate the productions of strange particles (Σ and Λ) and compare the results to experimental data. Section 3 shows the results on the creation of non-strange particles. The UrQMD predictions for Ξ production are given in section 4. Finally, in section 5, we conclude our work.

2. UrQMD results on strange particle production

In this section, we use the UrQMD model [4–6] to calculate the yields, transverse momentum and rapidity spectra of strange particles in \bar{p} + nucleus collisions and compare the theoretical results with experimental data. The UrQMD approach is based on the covariant propagation of all incoming and secondary hadrons. It includes the annihilation of anti-baryons on baryons as well the subsequent interaction of strange particles with the nuclear matter.

The experimental study of \bar{p} + ${}^7\text{Li}$, ${}^{12}\text{C}$, ${}^{32}\text{S}$, ${}^{64}\text{Cu}$ collisions has been performed at the Serpukhov proton synchrotron with the RISK streamer chamber spectrometer [7]. An unseparated beam of negatively charged particles with momenta of 40 GeV/c is used as an incident beam composed of a mixture of π^- , K^- and \bar{p} in the ratio of 100:1.8:0.3. In the experiment, the average multiplicities of neutral hyperons, $\Lambda(\Sigma^0)$ and $\bar{\Lambda}(\bar{\Sigma}^0)$, were investigated in the following reactions:

$$\bar{p} + A \rightarrow \Lambda(\Sigma^0) + X, \bar{\Lambda}(\bar{\Sigma}^0) + X, \quad (1)$$

where A stands for ${}^7\text{Li}$, ${}^{12}\text{C}$, ${}^{32}\text{S}$ and ${}^{64}\text{Cu}$.

Shown in table 1 are our results as derived from the UrQMD model, compared with the experimental data. We find that the UrQMD results, for $\Lambda(\Sigma^0)$ and $\bar{\Lambda}(\bar{\Sigma}^0)$ production in the reactions \bar{p} + Li, C and S, slightly underestimate the experimental results (but are within the error bars), while for the \bar{p} + Cu reaction the UrQMD results slightly exceed the experimental data within the given errors. With increasing the mass of nuclear targets, the yields of $\Lambda(\Sigma^0)$ also increase while the multiplicities of anti-hyperons, $\bar{\Lambda}(\bar{\Sigma}^0)$, remain approximately constant. Considering the experimental errors, however, the UrQMD predictions for the averaged multiplicities of both $\Lambda(\Sigma^0)$ and $\bar{\Lambda}(\bar{\Sigma}^0)$ are in line with the experimental data.

Next, we focus on the production of Λ and K^0 in the reaction \bar{p} + ${}^{131}\text{Xe}$ at a \bar{p} beam energy of 200 GeV [8]. These experiments have been performed by the NA5 Collaboration at CERN SPS using a streamer chamber inside a 1.5 tesla superconductor vertex magnet. Table 2 shows the comparison between the NA5 experimental data [8] and UrQMD calculations on the average abundances of Λ , K^0 , negative hadrons (h^-), and the ratios $\langle n_{\Lambda} \rangle / \langle n_{h^-} \rangle$

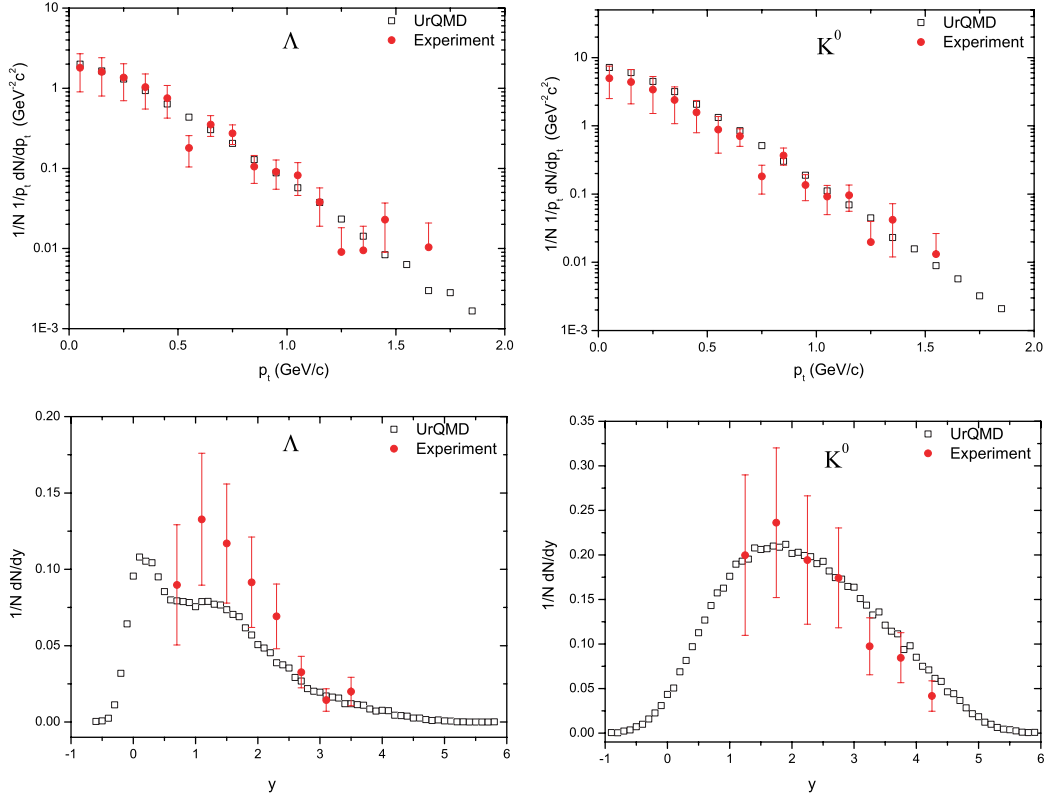


Figure 1. UrQMD results compared with experimental data [8] for transverse momentum distributions (upper panels) and normalized laboratory rapidity distributions (lower panels). Here Λ (left panels) and K^0 (right panels) are produced in $\bar{p} + \text{Xe}$ reaction at 200 GeV.

Table 2. Comparison between experimental data by the NA5 Collaboration [8] and UrQMD results on average multiplicities of Λ , K^0 , negative hadrons (h^-) and ratios.

	$\langle n_\Lambda \rangle$	$\langle n_{K^0} \rangle$	$\langle n_{h^-} \rangle$	$\langle n_\Lambda \rangle / \langle n_{h^-} \rangle$	$\langle n_{K^0} \rangle / \langle n_{h^-} \rangle$
Experimental	0.261 ± 0.04	0.610 ± 0.096	8.54 ± 0.15	0.031 ± 0.005	0.071 ± 0.011
UrQMD	0.228	0.695	8.54	0.027	0.081

and $\langle n_{K^0} \rangle / \langle n_{h^-} \rangle$. Again, one observes that the UrQMD calculations provide a satisfactory description of the experimental results.

To obtain more insights, we compare UrQMD results with experimental data for the transverse momentum distributions and normalized laboratory rapidity distributions ($\frac{1}{N} \frac{1}{p_t} \frac{dN}{dp_t}$ and $\frac{1}{N} \frac{dN}{dy}$), with N being the number of events and p_t being the transverse momentum and y denoting the rapidity [8]. The transverse momentum distributions of Λ and K^0 are illustrated in figure 1 (upper panels). It appears that the UrQMD calculations slightly underestimate the Λ production at higher momenta (p_t larger than 1.2 GeV/c) while the K^0 production at low momenta (p_t less than 0.5 GeV/c) are slightly lower in UrQMD as compared to the data. Considering the large experimental errors, however, one can still conclude that the UrQMD calculation is in line with the experimental data.

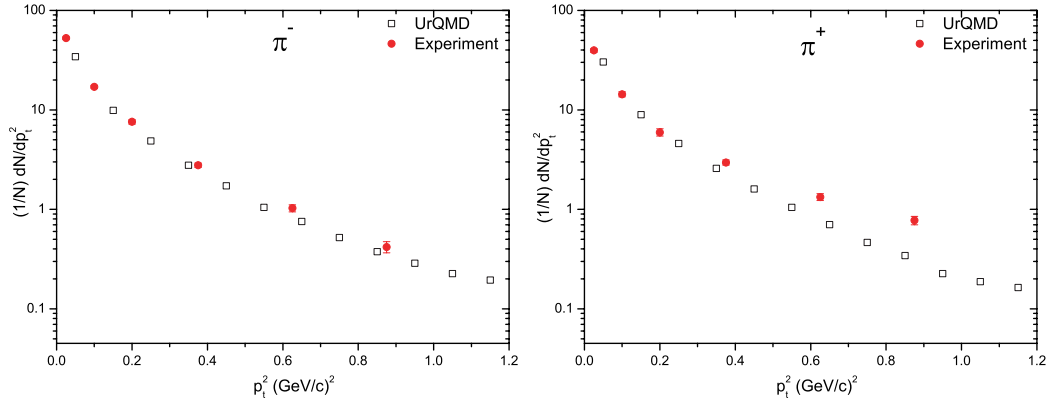


Figure 2. UrQMD results compared with experimental data [9] for p_t^2 distributions of π^- (left) and π^+ (right) produced in $\bar{p} + {}^{108}\text{Ag}$ at a \bar{p} momentum of 100 GeV/c.

The lower right panel of figure 1 depicts the comparison between experimental data and UrQMD results on the normalized laboratory rapidity distributions. It is found that the UrQMD result agrees with the experimental data for the K^0 production. The positively skewed, bell-shaped K^0 rapidity distribution reveals that K^0 are dominantly produced in the target fragmentation region. The Λ rapidity distribution in figure 1 (lower left panel) shows that the UrQMD calculations underestimate the yield of Λ in the central rapidity region. However, one should note that also here the experimental data suffer from substantial errors. The UrQMD predicted peak at $y \sim 0$ indicates that the ejection of Λ happens mainly in the target fragmentation region.

3. UrQMD results on non-strange particle production

Experimentally, reactions of $\bar{p} + {}^{24}\text{Mg}$, ${}^{108}\text{Ag}$ and ${}^{197}\text{Au}$ at \bar{p} momenta of 100 GeV/c have been performed at Fermilab in the experiment E597 with the Fermilab 30 inch bubble chamber and downstream particle identifier (DPI) to study the production of inclusive charged pion spectra [9]. To compare to this data, we employ the UrQMD model and explore the production of π^\pm in the reactions:

$$\bar{p} + \text{Mg, Ag, Au} \rightarrow \pi^\pm + X. \quad (2)$$

The comparison between the experimental data and the UrQMD predictions on p_t^2 distributions is shown in figure 2. Due to the limited space we restrict ourselves to the π^\pm production from $\bar{p} + \text{Ag} \rightarrow \pi^\pm + X$ reactions since the results for Mg, Ag and Au targets are quite similar. Figure 2 clearly shows that the UrQMD calculations agree well with the experimental data on the transverse momentum spectra of π^- , in the case of π^+ a slight deviation from the data is observed toward high p_t^2 . However, one may note that π are mainly produced at low momenta.

4. Model predictions for $\Xi\bar{\Xi}$ production

As seen in sections 2 and 3, UrQMD reproduces the experimental data of strange and non-strange particles reasonably well. Thus, one can conclude that the UrQMD model is a suitable tool to predict strange particle spectra and abundancies in antiproton–nucleus collisions. In

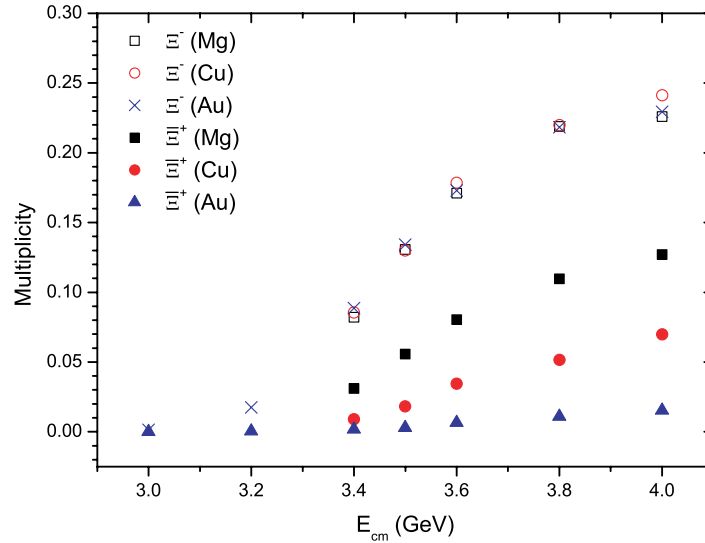


Figure 3. Multiplicities of Ξ^- and Ξ^+ from the reactions of $\bar{p} + \text{Mg, Cu and Au}$ collisions.

this section, we employ the UrQMD model to provide information of productions of the multi-strange hyperons $\Xi\bar{\Xi}$ which are the important ingredients for double Λ hypernuclei formation. Figure 3 depicts the multiplicities of Ξ^- and Ξ^+ as calculated in the UrQMD model for the reactions $\bar{p} + {}^{24}\text{Mg}$, ${}^{64}\text{Cu}$ and ${}^{197}\text{Au}$ at center-of-mass energies from 3 to 4 GeV. It is found that the multiplicities of Ξ^- are very similar for the different targets but significantly increase with increasing center-of-mass energy. The multiplicities of Ξ^+ are considerably different for different reactions. The multiplicity of Ξ^+ produced with the Mg target is clearly higher than Ξ^+ from the Cu target, and the multiplicity of Ξ^+ from the Au target is almost zero for the whole inspected energy region. This observation can be well understood, because a bigger-sized nucleus provides a higher chance for Ξ^+ to be absorbed by subsequent collisions with the nucleons. The predicted multiplicities provide useful information for the trigger condition for double Λ hypernuclei production.

5. Summary

Within the UrQMD model we have calculated the multiplicities of $\Lambda(\Sigma^0)$ and $\bar{\Lambda}(\bar{\Sigma}^0)$ (anti-) hyperons produced in $\bar{p} + A$ collisions at 40 GeV/c and found that the theoretical results are consistent with the experimental data. The UrQMD calculations also reproduce quite well the experimental data for the production of Λ , K^0 and negatively charged hadrons (h^-) in the reaction $\bar{p} + \text{Xe}$ at a \bar{p} momentum of 200 GeV.

The UrQMD calculations reproduce well the experimental data for the transverse momentum distributions of Λ and K^0 and the theoretical results are also in line with the data for the normalized lab rapidity distributions. The positively skewed curves in figure 1 for the rapidity distributions of both Λ and K^0 indicate that the particles are mainly produced in the target fragmentation region, and the dominant production of Λ at $y \sim 0$ suggests that a large number of the particles are produced in the transverse direction. The UrQMD results on pion production in the reactions $\bar{p} + \text{Mg, Ag and Au}$ are found to be consistent with the experimental data, too. Finally, we have calculated the multiplicities of hyperons $\Xi\bar{\Xi}$

in different reactions. These predictions are helpful to estimate the trigger conditions in the planned double Λ hypernuclei experiments.

Acknowledgments

This work is supported by the Commission on Higher Education, Thailand (CHE-RES-RG Theoretical Physics). The computational resources have been provided by the Thai National Grid Center. AL acknowledges support from Suranaree University of Technology. This work was supported by BMBF and GSI.

References

- [1] Amsler C *et al* and Particle Data Group 2008 *Phys. Lett. B* **667** 1
- [2] Conceptual design report: an international accelerator facility for beams of ions and antiprotons, <http://www.gsi.de/GSI-Future/cdr>
- [3] Pochodzalla J 2005 *Nucl. Phys. A* **754** 430
- [4] Bass S A *et al* 1998 *Prog. Part. Nucl. Phys.* **41** 255 (arXiv:nucl-th/9803035)
- [5] Bleicher M *et al* 1999 *J. Phys. G: Nucl. Part. Phys.* **25** 1859 (arXiv:hep-ph/9909407)
- [6] Petersen H, Bleicher M, Bass S A and Stöcker H arXiv:0805.0567 [hep-ph]
- [7] Grigalashvili T *et al* 1999 *Eur. Phys. J. C* **10** 265 (arXiv:hep-ex/9803016)
- [8] Derado I, Kadija K, Malecki M, Schmitz N and Seyboth P 1991 *Z. Phys. C* **50** 31
- [9] Whitmore J J *et al* 1994 *Z. Phys. C* **62** 199

CURRICULUM VITAE

NAME Mr. Ayut Limphirat
DATE OF BIRTH May 10, 1981
PLACE OF BIRTH Ratchaburi, Thailand
PERSONAL ADDRESS 40/2 M.7, Khao-Cha-Ngum Sub-district,
Photharam district, Ratchaburi 70120, Thailand
Tel. 66-32-740025, Mobile. 66-86-5082819
E-MAIL limphirat@yahoo.com, ayut2002@hotmail.com

EDUCATIONS

Degree of Doctor of Philosophy (2005 - present)

School of Physics, Suranaree University of Technology, Nakhon Ratchasima,
Thailand

Title of Thesis: Simulation of hypernucleus production in hyperon induced
reactions

Supervisors: Asst. Prof. Dr. Chinorat Kobdaj and Prof. Dr. Yupeng Yan

Master of Science (2002 - 2004)

School of Physics, Suranaree University of Technology, Nakhon Ratchasima,
Thailand

Supervisors: Dr. Chinorat Kobdaj and Assoc. Prof. Dr. Yupeng Yan

Bachelor of Science (1998 - 2001)

Department of Physics, Chulalongkorn University, Bangkok, Thailand

Supervisor: Assoc. Prof. Dr. Phatana Phavanantha